Journal of Sound and Vibration 595 (2025) 118771

Contents lists available at ScienceDirect

Journal of Sound and Vibration

journal homepage: www.elsevier.com/locate/jsvi

Shape considerations for the design of propellers with trailing edge serrations

Jorge Santamaria [a,*], André Bierrenbach-Lima [a,c], Marlène Sanjosé [a], Stéphane Moreau [b]

[a] École de Technologie Supérieure, Mechanical Engineering, 1100 rue Notre Dame Ouest, Montréal, H3C 1K3, Québec, Canada
[b] Université de Sherbrooke, Mechanical Engineering, 2500 boulevard de l'Université, Sherbrooke, J1K 1T1, Québec, Canada
[c] Institut Supérieur de l'Aéronautique et de l'Espace, 10 Av. Edouard Belin, Toulouse, 31400, France

ARTICLE INFO

Keywords:
Trailing edge noise
Serrations
Propeller

ABSTRACT

Noise reductions due to trailing edge serrations of several representative unmanned air vehicle propellers are calculated using a low-order methodology based on RANS simulations coupled with an extension of Ayton's model proposed by Li and Lee, which provides a heuristic three-dimensional model for finite span applicable to rotor blades. The latter model is validated in the limit of zero serration amplitude against Amiet's and Schlinker and Amiet's models, finding good agreement at high frequencies for both airfoils and rotating blade elements. Similar good validation results are obtained for finite serrations by comparing with experiments achieved on the Controlled Diffusion airfoil at Université de Sherbrooke, and with calculations for a serrated blade element by Tian and Lyu. The coupled methodology is then validated both aerodynamically and acoustically with ISAE measurements for a representative drone propeller at different rotational speeds. The corresponding serrated model is then used to calculate noise reductions caused by different shapes. The square wave serration is shown to outperform the sawtooth and sinusoidal shapes for all frequencies and observer angles for small propeller blades typically used for drones. Yet, for larger chord blades typically used for ducted fans, combinations of sawtooth and sinusoidal serrations provide better noise reductions.

1. Introduction

Trailing edge noise (TEN) is a by-product of the flow over airfoils and blades and is the dominant propeller broadband noise mechanism under homogeneous steady inflow conditions, e.g., while hovering [1,2]. The proliferation of unmanned aerial vehicles (UAV) and the potential introduction of Urban Air Mobility (UAM) vehicles pose many challenges for the aeronautics community. Among them is the noise emission from the propeller. The relatively low Reynolds number in which UAV operates adds further challenges to predicting and mitigating TEN [3]. While the use of the Ffowcs-Williams & Hawkings acoustic analogy with results from high-fidelity simulations such as Lattice-Boltzmann/Very-Large Eddy Simulation [1,4] now permit the calculation of UAV/UAM trailing-edge noise, their high computational cost puts them at the end of the design cycle rather than at the beginning. Thus, propeller designers could benefit from low-order methodologies during early design phases or for surrogate-based optimization.

Bio-inspired modifications such as serrations, brushes, and porous edges have shown the potential to reduce airfoil and propeller trailing edge noise [5], with serrations being the favored passive method in turbomachinery. While Oerlemans et al. [6] pioneered the use of serrations for wind turbines, their use in propellers is more recent. For example, Ning et al. [7] found that using sharp

* Corresponding author.
E-mail address: jorge-hernan.santamaria-osorio.1@ens.etsmtl.ca (J. Santamaria).

https://doi.org/10.1016/j.jsv.2024.118771
Received 28 March 2024; Received in revised form 8 October 2024; Accepted 9 October 2024
Available online 10 October 2024

serrations reduced propeller TEN at one observer location without significantly impacting global aerodynamics. Similar results for more observers upstream of the propeller were measured by Pang et al. [8]. Later, Yang et al. [9] found no difference in having half-span versus full-span serrations, additionally investigating the influence of serration manufacturing method in aerodynamics and acoustics. While there is sufficient experimental evidence that serrations can reduce propeller TEN, the theoretical models are still in their infancy [10], and the necessary simplifications made to obtain closed-form solutions are ongoing research.

The process by which a minute fraction of the turbulence kinetic energy within the boundary layer is converted to noise at the trailing edge was heavily studied following Lighthill [11] seminal work, with Powell [12] showing a $\approx U^{4-5}$ scaling of the acoustic power with the flow velocity. During the seventies, Ffowcs Williams and Hall [13], Howe [14] and Amiet [15] derived analytical models from first principles to predict trailing edge noise. All models agree with Powell's scaling and yield a dipole-type directivity pattern. A detailed account for these TEN models can be found in [5] (section 2). Brooks et al. [16] (BPM) then proposed a simpler empirical model to calculate airfoil self-noise, including TEN. The model is based on scaling laws for TEN and empirical fitting using several measurements on NACA0012 airfoils at different operating parameters [17]. The main drawback of the method is when it is used for airfoils that differ significantly from the NACA0012 shape [5]. Later, Roger and Moreau [18] extended Amiet's model to include the effects of backscattering from the leading edge which are important at small non-dimensional frequencies. In the latter physics-based model, a relationship exists between the source, i.e., the wall-pressure fluctuations close to the trailing edge, and the far-field acoustic pressure [5,14]. Direct measurement of the former is difficult for any rotating machinery [19]. Thus, a key step of TEN prediction is the modeling of the wall-pressure fluctuations spectrum. Since the local pressure field in an incompressible boundary layer depends on the velocity field over the whole domain [20], this task is not trivial. One approach uses Poisson's equation that relates the pressure and velocity fields. Provided the turbulent field is found homogeneous in planes parallel to the wall, Panton and Linebarger found a solution of this inhomogeneous equation in the form of a quintuple integral that can only be solved efficiently with a Monte Carlo method. A simplified version of it is the TNO-Blake model, which also uses information on the mean shear profile and the vertical velocity spectrum to yield the wall-pressure spectrum. Yet, this approach still requires the approximation of a multiple integral [5] and might not be ideal for fast calculations. A faster alternative is based on a semi-empirical approach where the one-point wall-pressure spectrum is modeled based on a universal spectrum shape, requiring only local characterization of the boundary layer. Goody [21] used measurements over a zero-pressure gradient turbulent boundary layer to propose an empirical wall-pressure model with Reynolds number effects. Further developments included the effects of adverse [22] and favorable pressure gradients [23].

Direct Numerical Simulations (DNS) [24–26] have shown that the far-field noise reduction achieved by serrations is caused by the scattering process, i.e., tip-root interference rather than a change in the turbulence statistics. This minimal change in turbulence statistics between straight and serrated edges can be exploited by modeling the wall-pressure spectrum only once and using analytical models to account for the scattering differences between straight and serrated edges. In this study, fast, single-passage Reynolds-averaged Navier–Stokes simulations are used to model the wall-pressure fluctuations spectrum at the trailing edge [27,28]. Howe [29] was the first to propose a modified TEN model to predict noise reduction due to serrated edges; however, experimental findings [30] disagreed with theoretical results. Lyu et al. [31] identified an incorrect Green's function as the source of disagreement and used a Fourier expansion and Amiet's solution iteratively to solve the serrated edge problem, improving the noise reduction predictions. Later, Ayton [32] used the Wiener–Hopf method to solve the boundary value problem and found a closed-form solution involving a sum over a finite number of modes [33].

The analytical computation of propeller trailing edge noise often relies on Schlinker and Amiet [34] method, which has been validated theoretically [35] and experimentally [36]. In essence, the method uses a blade strip approach to compute the rotor TEN by a weighted average of the acoustic pressure over one revolution. For serrated propellers, Halimi et al. [37] used Lyu et al. [31] first-order solution coupled with Schlinker and Amiet's method, finding fair agreement with LBM calculations, but pointing out the need for further investigations for order-convergence and number of modes required. More recently, Tian and Lyu [10] showed that at most second order was necessary for convergence and found that the Doppler effects are minimal at low Mach numbers and the directivity patterns depended mostly on the isolated airfoil patterns. Li and Lee [38] heuristically extended the rapid Ayton's model to use it for propellers, and while the agreement with experiments is not perfect, the model gives insight into possible noise reductions. The original model of Ayton [32] states how different serration geometries perform better at different frequency ranges. In this paper, this fact is exploited for a propeller with different serration patterns along the span.

The present study provides a low-order methodology to predict noise reductions for a representative drone propeller with serrations. The method uses RANS simulations to model the wall-pressure statistics, the extended Ayton's model to calculate the blade strip far-field noise, and Schlinker and Amiet's method for the complete rotor far-field noise. Section 2 presents the theoretical models and their limitations. The validation of the extended Ayton's model for airfoils and rotating blades follows in Section 3. In Section 4, the proposed methodology is applied to a typical drone propeller to calculate the potential noise reductions by using different shapes. Section 5 then provides a parametric study to more general UAVs. Conclusions and perspectives are drawn in Section 6.

2. Modeling of trailing edge noise

This section presents the mathematical models for predicting trailing-edge noise from airfoils and/or blade segments and their corresponding extension to rotating blades. Fig. 1 shows the airfoil coordinates.

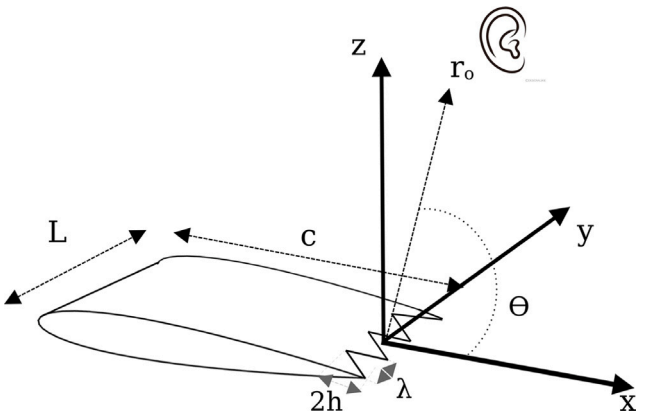

Fig. 1. Blade strip (local) coordinates.

2.1. Straight edge

For straight edges, Amiet's model [15,39] is used. The latter assumes a pressure disturbance convected by a uniform flow with velocity U in the x direction along a half-plane that models an infinitesimally thin airfoil with its edge aligned with the y axis. The disturbance is responsible for the unsteady loading on the half-plane, and by using the linearized Euler equations, it is possible to obtain a Helmholtz equation in terms of the pressure. The boundary value problem (BVP) then requires two boundary conditions, one upstream of the edge and one downstream. The no-flow-through condition must be satisfied in the former case and the Kutta condition in the latter. The validity and importance of the Kutta condition for aeroacoustics has been discussed in [40]. Amiet proceeded to solve the BVP by using the Schwarzschild solution, which was originally used in electromagnetic diffraction problems. The solution yields the pressure (loading) distribution on the plane and it is assumed to be an equivalent dipole noise source. The acoustic propagation of the noise source to the far-field is obtained by integrating along the plane's surface using Curle's analogy [41]. Statistical considerations of the hypothetical boundary layer developing over the plate are required to model the turbulence and obtain a close form for the acoustic pressure power spectral density (PSD) at a given angular frequency ω, and observer position $\mathbf{r_o}$:

$$S_{pp}(\omega, \mathbf{r_o}) = \underbrace{\left(\frac{kcz}{4\pi S_0^2}\right)^2 2\pi L}_{1} \underbrace{\left| I\left(\frac{\omega}{U_c}, k\frac{y}{S_0}\right)\right|^2}_{2} \underbrace{\Pi_0\left(\frac{\omega}{U_c}, k\frac{y}{S_0}\right)}_{3} \tag{1}$$

Eq. (1) has three terms. The first one is a directivity factor depending on the acoustic wavenumber k, the airfoil strip chord c, and span L, the observer position normal to the airfoil z, and the convection-corrected observer distance $S_0^2 = x^2 + \beta^2(y^2 + z^2)$. The second term is the aeroacoustic transfer function found by integrating the source term, which depends on the convection velocity of turbulent eddies U_c, taken as $0.7\,U$ in this paper, and the spanwise wavenumber $k_y = k\,y/S_0$. Expressions for the aeroacoustic transfer functions can be found in Appendix A. Lastly, the wall-pressure wavenumber–frequency spectrum Π_0 contains the energy of the pressure fluctuations beneath the boundary layer. The latter term is not usually known and must be either measured, simulated, or modeled. The term Π_0 contains a vast amount of information [18] and for practical engineering calculations can be approximated using Corcos' model [42]:

$$\Pi_0\left(\frac{\omega}{U_c}, k\frac{y}{S_0}\right) = \frac{1}{\pi}\,\phi_{pp}(\omega)\,l_y\left(\omega, k\frac{y}{S_0}\right) \tag{2}$$

where $\phi_{pp}(\omega)$ is the local wall-pressure spectrum and l_y is the spanwise correlation length of wall-pressure fluctuations for which the simplified Corcos' model can be used:

$$l_y\left(\omega, k_y\right) = \frac{\omega/(b_c U_c)}{k_y^2 + \omega^2/(b_c U_c)^2} \tag{3}$$

with b_c, the inverse of the exponential decay rate of the spanwise coherence function, which is fixed to 1.47 in this paper. In the absence of measurements or numerical simulations, the wall-pressure spectrum can be modeled by using semi-empirical models based on experimental measurements and theoretical developments [5]. For flat plates at an angle of attack, the simple model of Chou and George [43] can be used:

$$\phi_{pp}(\omega) = \left(\frac{1}{2}\rho U^2\right)\frac{\delta^*}{U}F(\bar{\omega}) \tag{4}$$

where ρ is the fluid density, δ^* is the boundary layer displacement thickness and $\bar{\omega} = \omega\delta^*/U$.

More sophisticated wall-pressure models can be found in the literature [23] and in the present study, Lee's extension of Rozenberg's [22] model is used

$$\phi_{pp}(\omega)SS = \frac{a(\omega FS)^b}{[i(\omega FS)^c + d]^e + [(fR_T^g)(\omega FS)]^h} \tag{5}$$

where R_T is the ratio of timescales between the outer and inner boundary layer sides given by $(\delta/U_e)/(\nu/u_\tau)$ that characterizes the Reynolds number effect. Note that other models may use the boundary-layer displacement thickness δ^* instead of the boundary-layer thickness δ. Additionally, U_e is the boundary-layer edge velocity, ν is the kinematic viscosity and $u_\tau = \sqrt{2\tau_w/\rho}$ is the friction velocity with τ_w being the wall shear stress. SS and FS represent the spectrum scale factor and the frequency scale factor, respectively. The values of the parameters used in Rozenberg's and Lee's model can be found in Appendix B.

2.2. Serrated edge

Modeling serrated edges is more involved than straight edges, albeit the BVP is rather similar between the two cases. The only difference is the physical boundary determining the edge between the slip and Kutta conditions. While many efforts [29,31] have focused on sawtooth trailing edges, it is possible to have any piecewise function to describe the geometric pattern of the edge. In general, the serration tip-to-root amplitude is $2h$, and its wavelength λ. For example, Lyu et al. [31] used a non-orthogonal coordinate change and assumed the solution as a Fourier expansion, yielding a system of coupled PDEs. By iteratively using the Schwarzschild solution, an approximation of different orders can be found, with a second-order solution giving reasonable convergence [31,37]. Later, Ayton [32] used the Wiener–Hopf method to obtain a closed form of the mixed BVP. Ayton used the same non-orthogonal coordinate transformation as Lyu but noted that the traditional method of separation of variables could be used by Fourier transforming the coupled streamwise and spanwise coordinates. This resulted in an eigenfunction expansion for the spanwise direction, with corresponding eigenvalues depending on the spanwise wavenumber. The expansion coefficients are found by application of the standard Wiener–Hopf method. To obtain a closed-form solution for the far-field acoustic pressure, Ayton applied the method of steepest descent (or stationary phase) to approximate the inverse Fourier Transform. The resulting equation still required the numerical approximation of an integral. Later Lyu and Ayton [33] noted that the integral could be reduced to a sum for sharper serrations fulfilling the condition $k\lambda/\beta < 2\pi$. The rapid Lyu and Ayton's model then reads:

$$S_{pp}^A(\omega, \mathbf{r_o}) \approx \frac{k\beta}{4\pi^2 S_0} \frac{\chi + \bar{k}}{(\chi - \bar{k}\cos\Theta)^2} \sin^2\left(\frac{\Theta}{2}\right) \phi_{pp}(\omega) \sum_{n=-\infty}^{+\infty} |E_n(\Lambda)|^2 l_y\left(\omega, \frac{2\pi n}{\lambda}\right) \tag{6}$$

where $\chi = \bar{k}_x\beta$ is the corrected reduced aerodynamic streamwise wavenumber with $\bar{k}_x = \omega/U_c + kM/\beta^2$ and Θ is the observer angle measured from the streamwise direction (see Fig. 1). Note that Corcos' model given by Eqs (2) and (3) has been used to obtain the expression in terms of ϕ_{pp} and l_y. The modal expansion coefficients E_n are analogous to the aeroacoustic transfer function and depend on the geometry of the serration, $F(y)$.

$$E_n(\Lambda) = \int_0^1 e^{i\Lambda F(y)} e^{-i2\pi n y} dy \tag{7}$$

where $\Lambda = (\bar{k}_x - \bar{k}\cos\Theta)2h/\beta$. This coefficient regulates the degree of interference between the serration tip and root [32], thus dictating the noise reduction capabilities of each shape. Expressions for the sawtooth, sinusoidal, and square wave modal expansion coefficients can be found in Appendix A and in Ayton and Chaitanya [44] for more shapes. Note that the original formulation for the expansion coefficients in [32] is used in this paper to avoid a scaling issue found in [45].

In practice, only a finite number of modes are considered for the evaluation of the modal expansion coefficients in Eq. (6) [26,38] and the zeroth-mode, $E_0(\Lambda)$, dominates the root-to-tip interference effect, thus giving a good overview of the noise reduction capabilities for each shape. Fig. 2 shows the magnitude squared of the zeroth-mode expansion coefficient for the sawtooth, sinusoidal, slitted-V, and square wave taking an observer at 90°. Firstly, it is observed that for sufficiently low values of Λ the square wave outperforms all other shapes. Secondly, for values of Λ close to 10, the square wave becomes ineffective and the sinusoidal shape outperforms for a small range of values before the sawtooth overtakes. The minima keep alternating between sawtooth and sinusoid for larger values of Λ. Lastly, it is shown that the slitted-V only outperforms the other shapes for very narrow ranges of Λ. The behavior of each shape thus can be exploited depending on the application type as will be shown in the next sections.

Both Lyu's and Ayton's models require some approximation to obtain a closed-form solution. This paper chooses the rapid Ayton's model due to its simpler final form and the possibility of handling different serration shapes. As noted by Tian and Lyu [10], the rapid Lyu and Ayton's model is a strictly two-dimensional model for an infinite span, and consequently, its radiated field is cylindrical as can be seen by the $1/S_0$ dependence in Eq. (6) as opposed to the expected $1/S_0^2$ decay in the far-field. Therefore, the 3D extension of the model is not straightforward; however, Li and Lee [38] heuristically modified the model to include the effects of finite span, propagation distance, and influence of spanwise observer. The extended Ayton's model then reads:

$$S_{pp}^{LL}(\omega, \mathbf{r_o}) \approx \frac{L\beta^2\bar{k}}{4\pi^2 S_0^2} \frac{\chi + \bar{k}}{(\chi - \bar{k}\cos\Theta)^2} \sin^2\left(\frac{\Theta}{2}\right) \phi_{pp}(\omega) \sum_{n=-\infty}^{+\infty} |E_n(-\bar{k}\cos\Theta)|^2 l_y\left(\omega, k_y\right) \tag{8}$$

where the airfoil strip span L and an additional observer distance term S_0 have been included. Additionally, the spanwise wavenumber is now $k_y = 2\pi n/\lambda + ky/S_0$. The factor of 4 in [38] is omitted in Eq. (8) for coherence with the previously defined

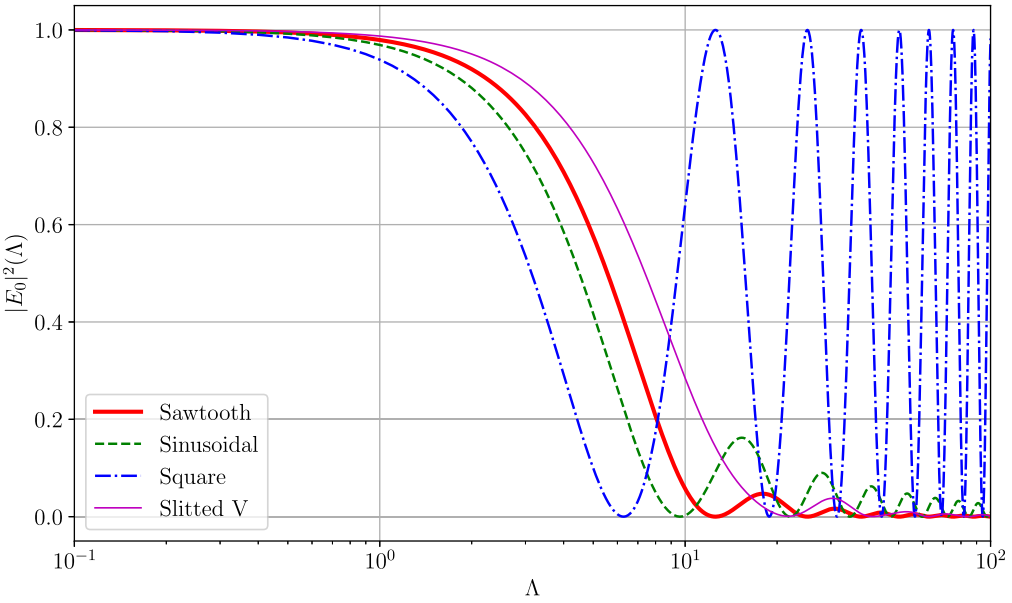

Fig. 2. Zeroth-mode expansion coefficients for different shapes.

Amiet's model in Eq. (1), which is a double-sided angular spectrum corresponding to a single boundary layer scattering at the flat plate trailing edge. Hence, once the calculation of either Eq. (1) or Eq. (8), the frequency spectrum is obtained by applying a factor of 8π corresponding to the appropriate 4 factor mentioned in [38] and the 2π factor corresponding to the conversion from angular frequency to frequency.

For the rest of the paper, Eq. (8) will be referred to as the extended Ayton's model.

2.3. Propeller trailing edge noise

Schlinker and Amiet [34] proposed a strip-theory-based method to use Amiet's model (Eq. (1)) for helicopter rotors, which was later successfully applied to low-speed fans [27,46], and more recently to wind turbines [47,48]. Let us consider a blade strip (green) rotating in the XY plane as shown in Fig. 3. This blade strip moves in a local rectilinear motion, thus neglecting the acceleration effects due to rotation. Additionally, the rotor frequency is much smaller when compared to the turbulence frequency, and the noise is blade-to-blade uncorrelated. Lastly, the noise from one blade strip can be obtained by a weighted average over one strip revolution, with the weight factor accounting for the Doppler effect for the emission frequency $\omega_e(\gamma)$. Thus, the PSD of the far-field acoustic pressure generated by the rotor reads:

$$S_{pp}^{\text{rotor}}(\mathbf{R_o},\omega) = \frac{B}{2\pi}\sum_{k=0}^{N_s}\int_0^{2\pi}\left(\frac{\omega_e(\gamma)}{\omega}\right)^2 S_{pp}^{\text{k}}\left(\mathbf{r_o},\omega(\gamma)\right)\mathrm{d}\gamma \tag{9}$$

with B the number of blades and N_s the number of blade strips. The integration variable γ sweeps the angular shift of the observers over a whole revolution ($0 \le \gamma \le 2\pi$). The Doppler shift is given by

$$\frac{\omega_e(\gamma)}{\omega} = 1 + \frac{M_t \sin\theta \sin(\gamma-\phi)}{\sqrt{1-\left(M_x \sin\theta\right)^2}} \tag{10}$$

where M_t and M_x are the blade strip tangential and axial Mach number respectively, with θ and ϕ the polar and azimuthal angles determining the observer's position in the rotor frame of reference. The full blade rotor noise is obtained by adding the contributions of all blade segments calculated with either Amiet's model (Eq. (1)) or the extended Ayton's model (Eq. (8)). The present study solves the integral in Eq. (9) numerically with the trapezoidal rule using 50 angular positions. The acoustic power radiated by the rotor can then be found by integrating Eq. (9) over a sphere S centered at the rotor hub center; in practice, a discrete number of observers is used. In this paper, 360 observers are used in the meridional plane (XZ plane in Fig. 3) and four observers in the azimuthal direction to obtain sufficient resolution without too much computational time.

$$\mathcal{P}(\omega) = \int_S \frac{S_{pp}^{\text{rotor}}(\mathbf{r_o},\omega)}{\rho_0 c_0}\mathrm{d}S \tag{11}$$

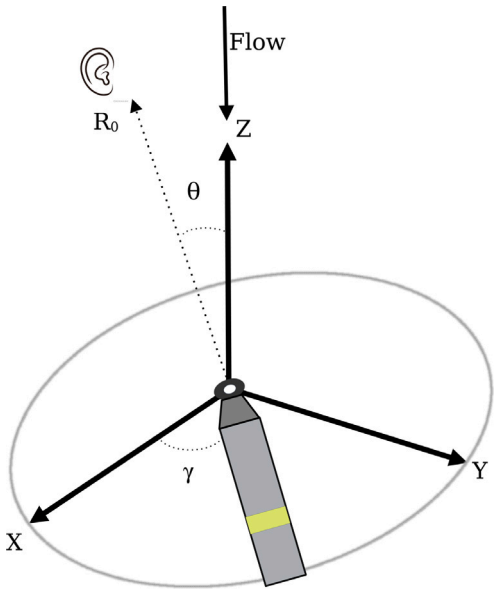

Fig. 3. Rotor (global) coordinates.

with $\rho_0 c_0$ being the air impedance at rest. The sound power level (SWL) in dB is computed from $\mathcal{P}$ for a resolution of $\Delta f = 1$ Hz and with a reference power of $W_{\text{ref}} = 10^{-12}$ W:

$$\text{SWL} = 10 \log_{10} \left(\frac{\mathcal{P}\, \Delta f}{W_{\text{ref}}} \right) \tag{12}$$

3. Validation and sensitivity analysis

The first part of this section presents directivity patterns for an industrial controlled-diffusion (CD) airfoil, for which abundant numerical and experimental data is available [24,49–51], using Amiet's model and the extended Ayton's model when the serration amplitude goes to zero. The models evaluate the directivity patterns for a representative wind turbine and cooling fan blade elements in the second part.

3.1. CD airfoil

Far-field acoustics, wall-pressure statistics, boundary layer, and wake profiles measurements were conducted at the anechoic wind tunnel at Université de Sherbrooke [52] and École Centrale de Lyon [51] on the CD airfoil at 8° and 16 m/s. The airfoil has a chord of 0.135 m and a span of 0.3 m, with a Reynolds number based on the chord of 1.5×10^5. A modular mockup of the CD airfoil has been built to test different passive noise control techniques [53]. Noise reduction obtained using smooth three-dimensional sawtooth serrations of size $2h = 10$ mm with an aspect ratio of 2 have been evaluated in the same flow conditions. Noise prediction using Direct Numerical Simulations have also been obtained on the straight and serrated CD airfoil for this configuration [24,26]. In the present work, DNS acoustic predictions are obtained using the Ffowcs Williams and Hawking's (FWH) analogy to avoid jet noise additional noise source [24] and provide a proper reference for the analytical models.

Fig. 4 compares experimental data from UdeS with Amiet's model extended to finite-chord given by Eq. (1), Lyu and Ayton's model given by Eq. (6) with a serration height set to zero, Li and Lee's extension given by Eq. (8) and the numerical predictions. It has been shown that wall-pressure statistics are fundamental to modeling trailing edge noise [5] accurately. Therefore, in the present validation case, the measured wall-pressure statistics are directly used in analytical models. In Fig. 4 (left), measured and predicted noise levels at 2 m from the trailing-edge in the $\Theta = 90°$ direction are shown for the baseline airfoil configuration with straight trailing-edge. In Fig. 4 (right), the noise level attenuation is computed by the difference in noise levels emitted by the airfoil with the serrated and the straight trailing edge.

Li and Lee's model (termed Ayton Extended) is seen to match Amiet's model at all but low frequencies, which is expected given the half-plane assumption involved in Lyu and Ayton's model [32]. Moreover, Li and Lee's model improves the agreement between the original Lyu and Ayton's model and Amiet's model as it automatically accounts for the finite span and the three-dimensional

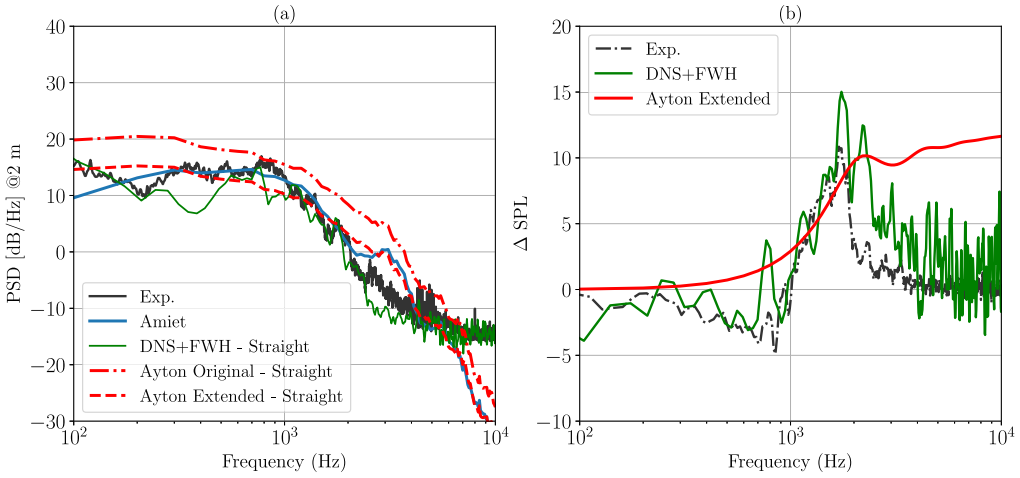

Fig. 4. (a) Acoustic pressure PSD for an observer at 2 m and 90° from the trailing edge for a straight edge airfoil and (b) SPL reduction with the use of serrations.

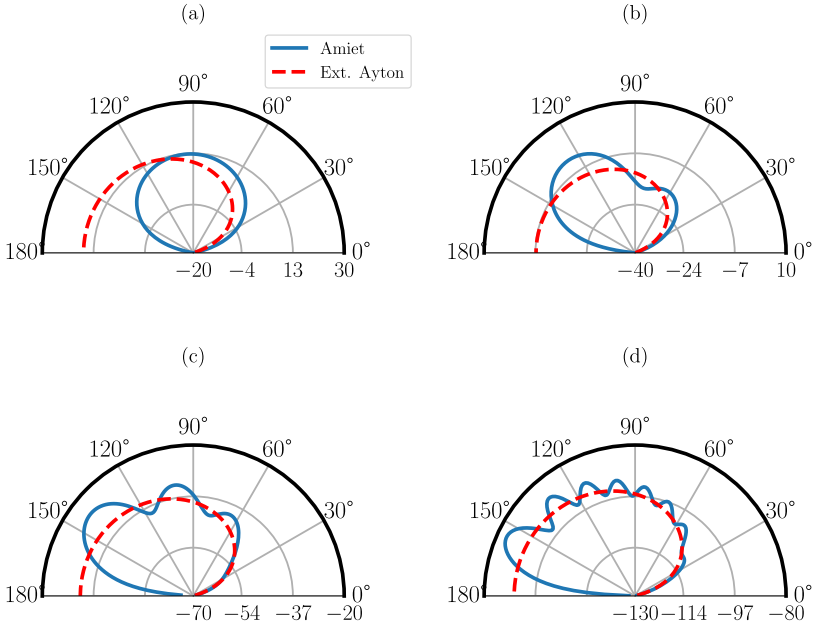

Fig. 5. SPL directivity for the CD airfoil using Amiet's and the extended Ayton's models. (a) $kc = 1$, (b) $kc = 5$, (c) $kc = 10$ and (d) $kc = 25$. The flow is from left to right.

noise radiation. Therefore, the ad-hoc scaling used by Moreau et al. [26] is no longer necessary. All analytical models follow the trends of the experimental data at mid to high frequencies. Only at high frequencies, does the experimental PSD at UdeS level out, as an additional wake noise source contributes to this frequency range [54,55]. Similar good trend of the noise reduction is observed for the serrated case. The difference seen beyond 4 kHz is again caused by the additional wake noise source. The extended Ayton's model therefore provides excellent airfoil noise predictions for both straight and serrated cases at $\Theta = 90°$.

Fig. 5 shows the directivity patterns for the CD airfoil using Amiet's model (Eq. (1)) and the extended Ayton's model (Eq. (8)) when the serration height, $2h$, approaches zero. It is clear that the extended Ayton's model matches the well-known half-plane solution, and the patterns are in perfect agreement with the finite chord and half-plane patterns in Howe [56] and Roger and Moreau [18]. Thus, it is expected that the extended Ayton's model gives good predictions for observers at 90° from the trailing edge, and discrepancies are expected at other observer positions.

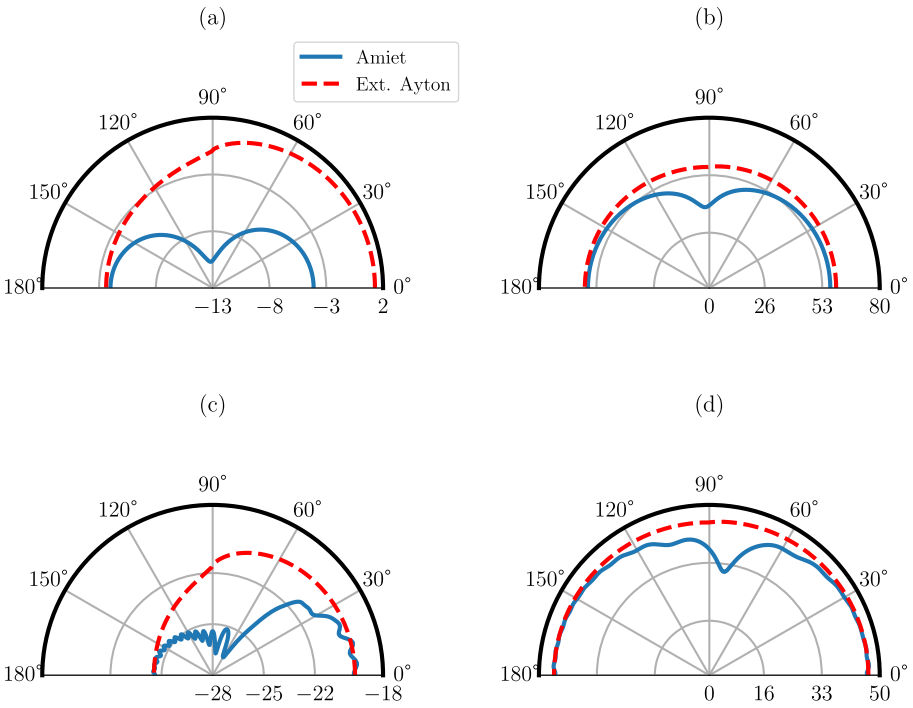

Fig. 6. SPL directivities for blade elements using Amiet's and the extended Ayton Model. (a) Cooling fan, $kc = 0.5$; (b) wind turbine, $kc = 0.5$; (c) cooling fan, $kc = 50$; and (f) cooling fan, $kc = 50$. The flow is from right to left.

Table 1
Parameters of the blade elements.

	Wind turbine	Cooling fan
Ω	25 RPM	600 RPM
Span	7.25 m	0.1 m
Chord	2 m	0.13 m
Pitch	10°	34°
Re_c	7.5×10^6	1.8×10^5
M_x	0.029	0.0354
M_t	0.165	0.0525

3.2. Rotating blade elements

Having established the directivity patterns of the extended Ayton's model for isolated blades, this section presents results on the representative wind turbine and cooling fan blade elements, first presented by Blandeau and Joseph [57] and later used by Sinayoko et al. [35] and Tian and Lyu [10] to validate Schlinker and Amiet's theory for rotating blades and for Lyu's serration model extension to rotating blades, respectively. The parameters of the blade elements are shown in Table 1. In both cases, Chou and George [43] wall-pressure spectrum is used (Eq. (4)). The free stream-to-convection velocity ratio, α, is assumed to be 1.25 and Corcos' constant, b_c, 1.61 following Sinayoko et al. [35].

Fig. 6 shows the directivity results for the cooling fan and the wind turbine at a low Helmholtz number, $kc = 0.5$, and a high one, $kc = 50$. The flow goes from right to left, so the rotational plane is at 90°. Firstly, it is noted that the implementation of Amiet's model is successful as the results are in good agreement with the directivity patterns in Sinayoko et al. [35]. Secondly, at high frequencies, it is clear that the extended Ayton's model matches Amiet's model for observers at high elevation angles from the rotational plane for both the cooling fan and the wind turbine, with the largest discrepancies occurring close to the rotational plane, as expected from the isolated airfoil directivity patterns from Fig. 5. In summary, it is expected that the extended Ayton's model will be valid for applications with sufficiently large chords ($kc \gg 1$), like wind turbines for all frequencies, whereas the validity for applications where the chord might be on the order of the acoustic wavelength ($kc \approx 1$) must be carefully assessed.

3.3. Sensitivity to serration shape

Given the behavior of the modal expansion coefficients over the range of the input Λ (Fig. 2), it is worth exploring how different shapes will perform for the representative cooling fan and wind turbine blade elements. Since detailed information on the boundary

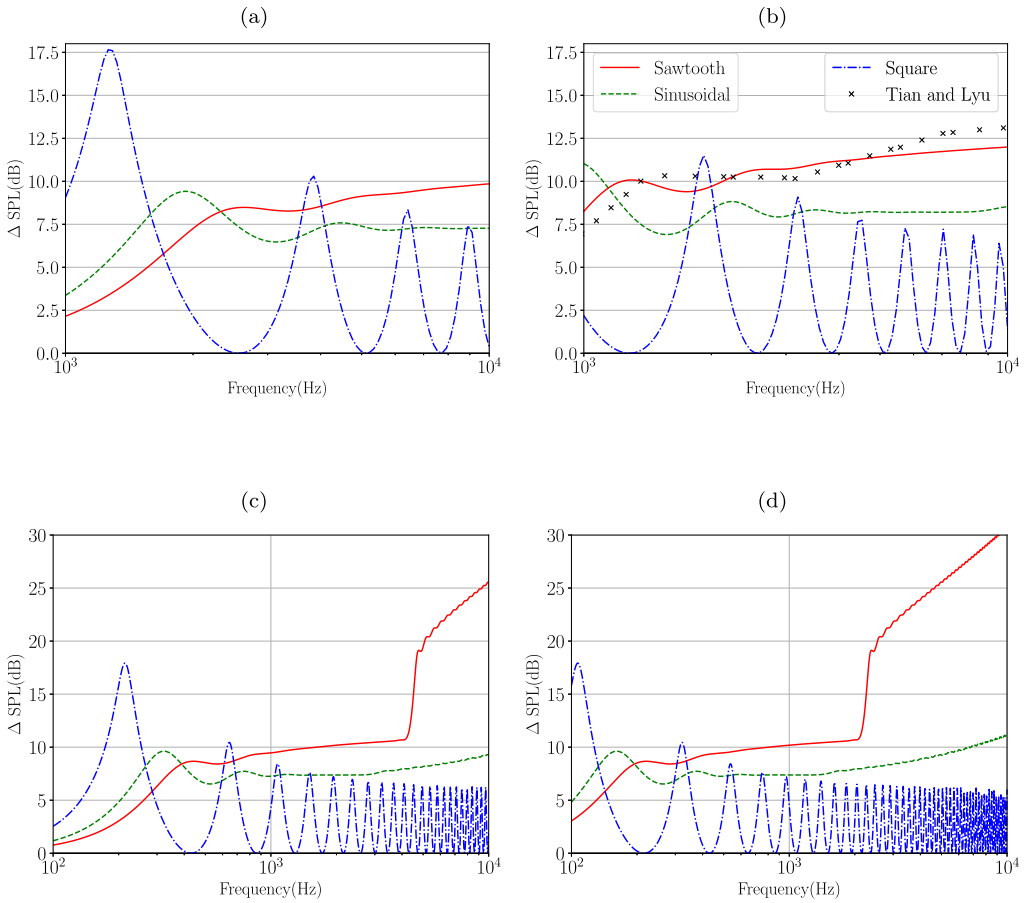

Fig. 7. Noise reduction for different serration shapes for the cooling fan and wind turbine blade elements computed at an observer at $\theta = 0°$, except for configuration (b) where the location is at $\theta = 45°$. (a) Cooling fan ($2h = 0.1\,c$), (b) Cooling fan ($2h = 0.2\,c$), (c) Wind Turbine ($2h = 0.1\,c$) (d) Wind Turbine ($2h = 0.2\,c$).

layer is not available for these cases, the largest serration amplitude considered is 20% of the chord to limit the impact on the aerodynamic performance. Fig. 7 shows the SPL reduction between straight edges and different serration shapes for the cooling fan and wind turbine elements. The serration amplitude-to-wavelength ratio ($2h/\lambda$) is fixed to 2, except for the cooling fan in Fig. 7(b) where it is 2.5 to allow comparison with the results in Tian and Lyu [10]. For this case an observer at $\theta = 45°$ is used, whereas for the other cases, the results are for an upstream observer given the good agreement for straight edges in Fig. 6 for both applications. The frequency range for the wind turbine is from 100 to 10 000 Hz and from 1000 to 10 000 Hz for the cooling fan.

It should be noted that the same conclusions from the zeroth-mode expansion coefficients in Fig. 2 apply for all cases. The square wave, sinusoidal, and sawtooth shapes outperform each other in different frequency ranges, but for all cases the sawtooth provides more consistent noise reduction and dominates over the other shapes as the serration height increases. For the cooling fan with a serration height of 10% of the chord, it is noted that the sinusoidal and sawtooth serrations outperform each other in relatively close frequency ranges. Thus it could be possible to use both shapes along the span to take advantage of their scattering properties. This arrangement will be investigated in the next sections. The large jump in the sawtooth case for the wind turbine is due to the decay rate of the expansion coefficients. For large argument, it can be shown that the sawtooth coefficients fall as $\approx 1/x$ whereas the sinusoidal coefficients fall as $\approx 1/\sqrt{x}$. Finally, the noise reductions for the wind turbine grow as $\log(2hk)$ in perfect agreement with the original model by Ayton [32]. These results show a fundamental limitation of the serrated models available in the literature as they do not account for the noise increase due to the flow through the serrations as reported experimentally [30].

4. Application to drone propellers

Having verified the frequency range and the directivity limitations of the extended Ayton's model, this section presents results for a representative drone propeller. The two-bladed rotor has a 0.25 m diameter (D), constant pitch (10°), and a constant chord (0.025 m) based on the NACA0012 airfoil. Experimental data from ISAE [58,59] are available for validation. The far-field acoustics are calculated following the methodology of Sanjosé and Moreau [60]. First, a single-passage RANS simulation of the rotor is

Fig. 8. Methodology for trailing-edge noise calculation.

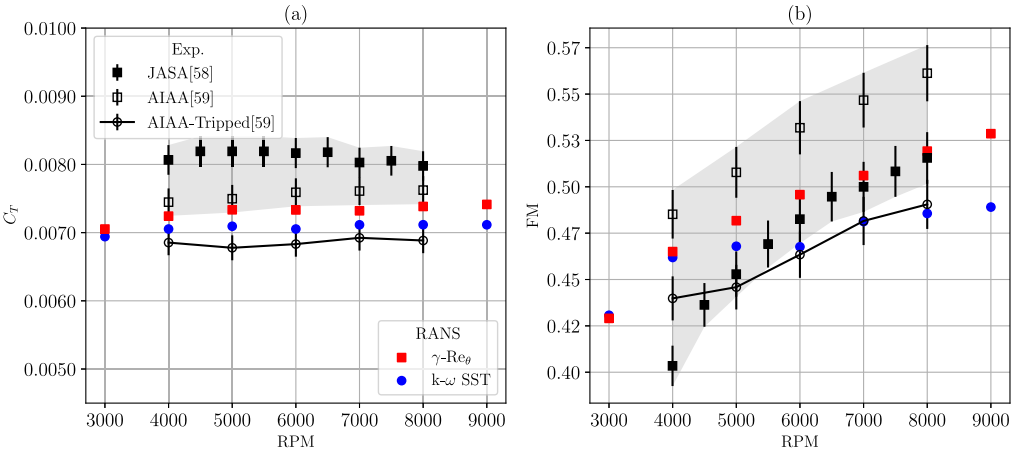

Fig. 9. Comparison of the thrust coefficient (a) and the Figure of Merit (b) calculated from RANS with experimental data.

performed. After the convergence of mean aerodynamic quantities, the blade is divided into strips, and boundary layer parameters are extracted. These parameters are used in the in-house broadband turbomachinery noise code PyFanNoise to model the wall-pressure spectrum and to calculate the far-field acoustic pressure using the models introduced and validated in Sections 2 and 3 for each strip. Lastly, the complete rotor far-field acoustic pressure at a given observer location is calculated. The methodology is summarized in Fig. 8.

4.1. Aerodynamic performance

RANS simulations of the isolated rotor in hover configuration from ISAE [58,59] are run using ANSYS CFX for the same rotational speed range [4000–8000 RPM]. The unstructured grid comprises prismatic elements for the boundary layer and tetrahedron for the rest of the domain for a total of 25 million elements. The meshing strategy follows the methodology by Ruiz et al. [61] in a similar low-Reynolds number propeller. Details of the mesh and the mesh convergence analysis can be found in Appendix C. The RANS equations are closed with k-ω SST turbulence model. Given that the flow over the blades is mostly transitional, in addition to fully-turbulent simulations, the γ - Re_θ model, based on the Langtry–Menter approach, is used to account for transitional flow effects. The computational domain consists of one stationary and one rotating domain using the frozen rotor formulation at the interface. Additionally, the dimensionless distance to the wall, y^+, is below 3 for most of the blade span in all cases and has maximum values at the leading edge of about 3, 4, and 5 for the 4000, 6000, and 8000 RPM cases respectively. Further simulation details can be found in Santamaria et al. [45].

Fig. 9 compares the thrust coefficient, $C_T = T/\rho(\pi R^2)(\Omega R)^2$, and Figure of Merit, $FM = C_T^{3/2}/\sqrt{2}C_Q$ calculated from the RANS simulations with two data sets. The first data set is from Gojon et al. [58] obtained using an SMD100 sensor on a test-rig located outside the anechoic room, while the second data set comes from Santamaria et al. [59] using a Nano 17 load cell on the test-rig inside the anechoic chamber. The latter data set also includes a propeller with tripping cylinders at 10% from the leading edge to force transition to turbulence on the blade suction side. First, note that there is a considerable variation between measurements on the same clean propeller as highlighted by the shaded areas. Secondly, the results for the transitional $\gamma - \mathrm{Re}_\theta$ and for the fully turbulent models are within the 95% confidence interval of the measured thrust and Figure of Merit values. Lastly, note that the prediction of static thrust remains challenging even for high-fidelity simulations with discrepancies between 5–12% [4,62,63].

A deeper insight into the rotor aerodynamics can be obtained with the mean wall-pressure contours and streaklines as shown in Fig. 10 for 4000, 6000, and 8000 RPM for the fully turbulent simulations. In addition, the same visualization is also shown for the transitional simulation at 6000 RPM. The pressure has been made dimensionless by the dynamic pressure taking as reference the blade's relative velocity at 75% of the span. The pressure distribution is the same in all cases, with the loading mostly concentrated in the last 25% of the span. The streaklines reveal the existence of radial flow on both the suction and pressure sides. The radial flow is stronger closer to the hub, affecting the whole suction side for the lowest velocity and less portions of the blade as the velocity increases. For the transitional results, the streaklines show much more radial flow on the suction side consistent with previous LES

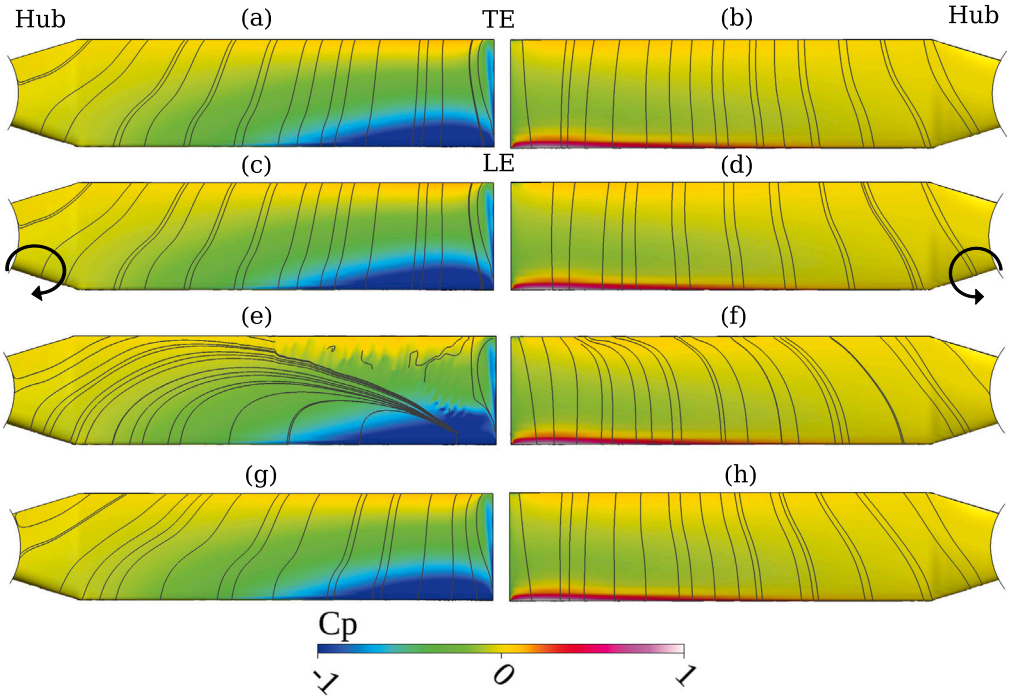

Fig. 10. Pressure coefficient contours and streaklines on the suction[(a),(c),(e) and (g)] and pressure [(b),(d),(f) and (h)] sides for various simulations: [(a),(b)] 8000 RPM, [(c),(d)] 6000 RPM, and [(g),(h)] 4000 RPM for fully turbulent cases, and [(e),(f)] 6000 RPM for the transitional case. (For interpretation of the references to color in this figure legend, the reader is referred to the web version of this article.)

results [64]. They also show the location of the transition to turbulence along the span as a result of laminar flow separation. The latter triggers the transition to turbulence at mid-chord in the outermost part of the blade, and thus the state of the boundary layer at the trailing edge is close to the fully turbulent case. Additionally, the influence of the tip vortex is noticed in all cases on the suction side as it disturbs the flow from the chordwise direction. Lastly, the streaklines in the fully turbulent cases show no evidence of flow detachment or recirculation.

Fig. 11 shows the turbulence kinetic energy (TKE) contours at mid-span and 90% span for the previous RPMs. For the fully turbulent results, the maximum TKE location is shown to be within the prismatic layer for all cases. This, along with the y^+ values obtained, assures that the inputs for the wall-pressure models are accurate. Additionally, note that the boundary layer of the 4000 RPM case presents very low levels of turbulence and it develops from the mid-chord, unlike the other two cases where the development starts around the quarter chord. Similarly, the transitional case remains laminar at midspan, and the transition triggered by the LSB at 90% span results the sharp increase of TKE and its thicker build-up all the way to the trailing edge.

With the results from the RANS simulations, the next step is the extraction of the boundary layer parameters to model the wall-pressure fluctuations spectrum. The extraction follows the same methodology based on the relative total pressure for the detection of the boundary layer edge as described by Sanjosé and Moreau [60], and it is performed at 85% of the chord. The evolution of some of the parameters required to model the wall-pressure spectrum is shown in Fig. 12 for different RPMs. The displacement thickness decreases as the speed increases as a direct consequence of increasing the Reynolds number. The curves for Clauser's parameter, β_c, tend to collapse for all rotational speeds along the midspan and diverge close to the blade tip, showing thus the independence of the Reynolds number in the midspan given that the chord at all radial positions is the same. Lastly, the wall shear stress, τ_w increases with Reynolds number as expected.

4.2. Acoustic results: straight edge

Following the extraction of the mean flow quantities along the span, the wall-pressure fluctuations spectrum $\phi_{pp}(\omega)$ and the far-field acoustic pressure PSD are calculated in PyFanNoise. Unless otherwise noted, Lee's model (8) is used in all calculations. After calculating the wall-pressure fluctuations spectrum and the blade strip acoustic pressure, the rotor acoustic PSD at a given observer location is computed from Eq. (9). The results for the propeller rotating at 6000 RPM obtained with the methodology described in Fig. 8 are shown in Fig. 13 and compared with experimental measurements from the clean and tripped propellers.

First, the impact of the turbulence modeling is assessed in Fig. 13 by investigating the results obtained with Amiet's model using fully turbulent (blue line) and transitional (green dashed line) results. Note that despite the different flow topology shown in Figs. 10 and 11 the far-field noise predictions are almost identical with minor differences in the low-frequency range as also observed

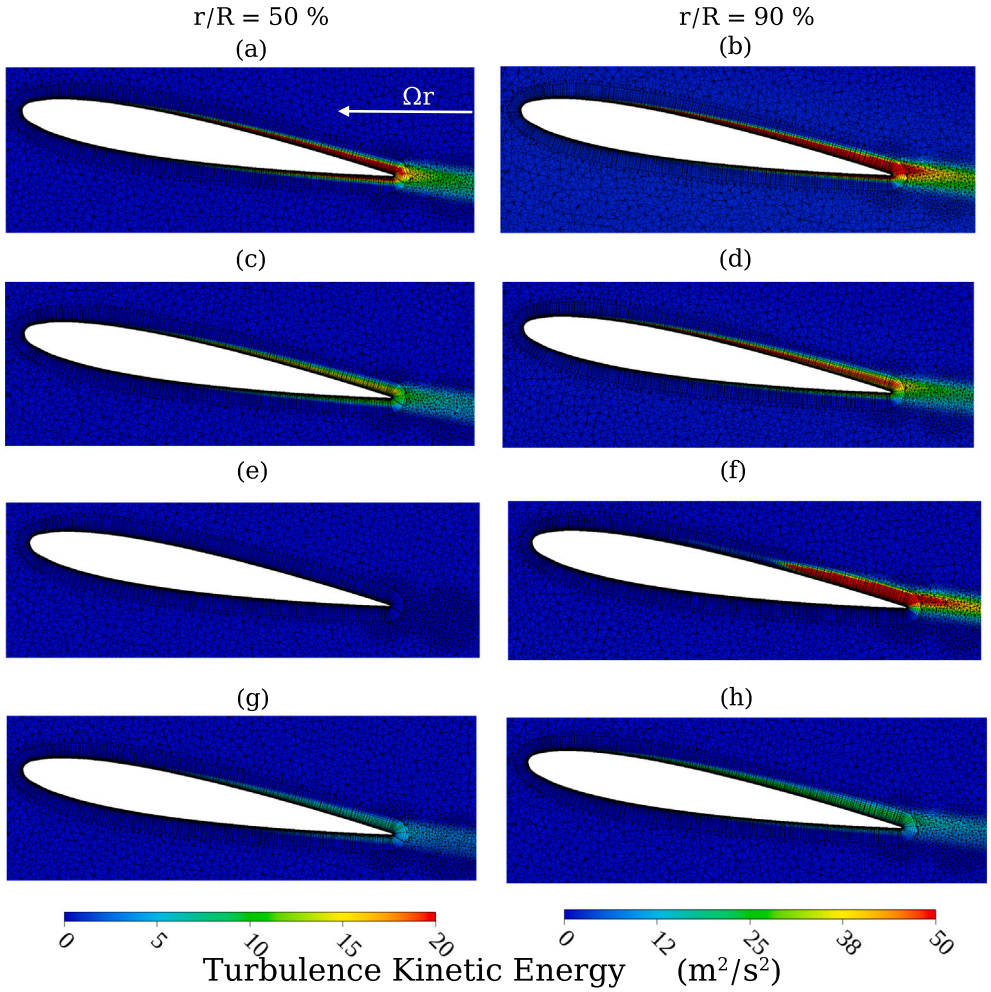

Fig. 11. Turbulence kinetic energy at 50% of the span [(a),(c),(e) and (g)] and 90% of the span [(b),(d),(f) and (h)] for various simulations: [(a),(b)] 8000 RPM, [(c),(d)] 6000 RPM, and [(g),(h)] 4000 RPM for fully turbulent cases, and [(e),(f)] 6000 RPM for the transitional case. (For interpretation of the references to color in this figure legend, the reader is referred to the web version of this article.)

experimentally. Since wall-pressure spectrum and correlation length model developments have been based on experimental data from fully developed turbulent boundary layers, only the results from the k-ω SST model will be used in the rest of the study.

Secondly, Amiet's model and the extended Ayton's model with serration height close to 0 are compared and good agreement in the trend is found between computations with identical strip number. The extended Ayton's model is seen to over-predict the sound power levels at low frequencies but matches Amiet's model at around 4 kHz, making the model valid in the frequency range where trailing-edge noise dominates. This is also consistent with the directivity analysis of Section 3. Lastly, note that both models underpredict the sound power levels for frequencies beyond 10 kHz. This is most likely caused by an additional noise source from a laminar boundary layer instability on the pressure side, as demonstrated in [65] where by tripping the pressure side only the high-frequency hump was removed and an early spectral roll-off around 4–5 kHz similar to the current prediction was observed. In the present study, only the noise caused by the scattering of fully turbulent boundary layers is considered, given the wall pressure spectrum modeling.

The calculated noise levels can be influenced by the number of strips selected to discretize the blade response. The calculation for the extended Ayton's model becomes independent of the number of strips at around 10 strips, as shown in Fig. 13. Similar results are obtained with Amiet's model as well (not shown here). It is important to note that while using more strips may seem to improve the matching with experimental data, the strip length cannot be arbitrarily small. The smallest strip length is limited by the spanwise correlation length, $l_y(\omega)$. Additionally, even though ten strips are used for the noise calculation, it is worth noting that approximately 95% of the acoustic power is radiated from the 2 outermost strips. Fig. 14 shows that strips 9 and 10 contribute the most to the total radiated acoustic power for a straight trailing edge, regardless of the model used.

Finally, a comparison of the directivity patterns obtained with Amiet's and Ayton's models with the experimental data from the tripped propeller is presented. The frequency range considered is 1–16 kHz as in the experimental campaign, where the broadband

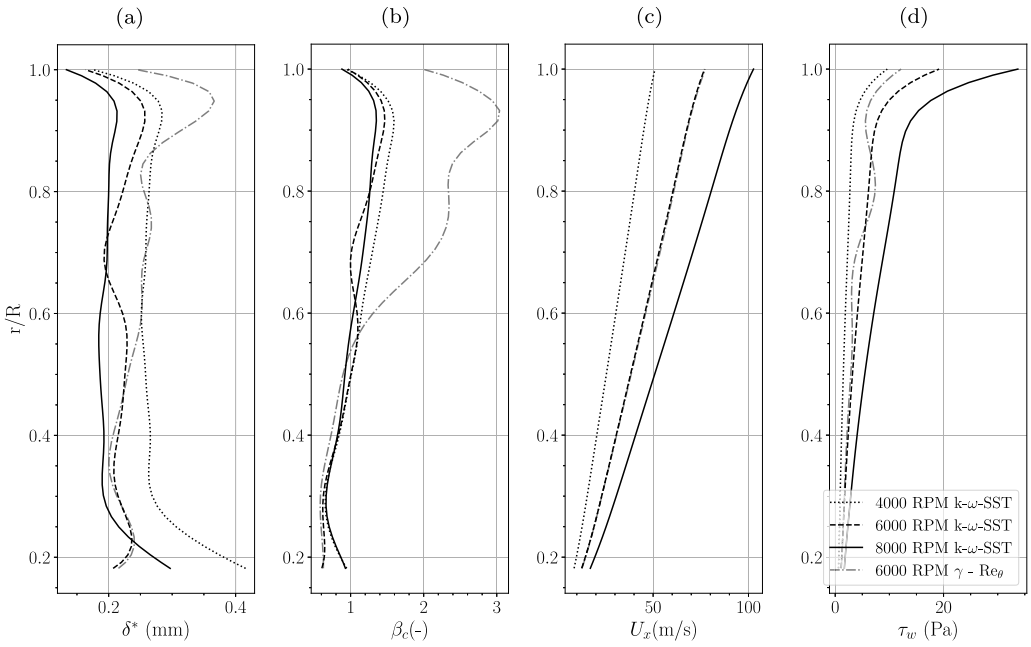

Fig. 12. Evolution of the boundary layer displacement thickness (a), Clauser's parameter (b), external velocity (c), and wall shear stress (d) along the span for different RPMs.

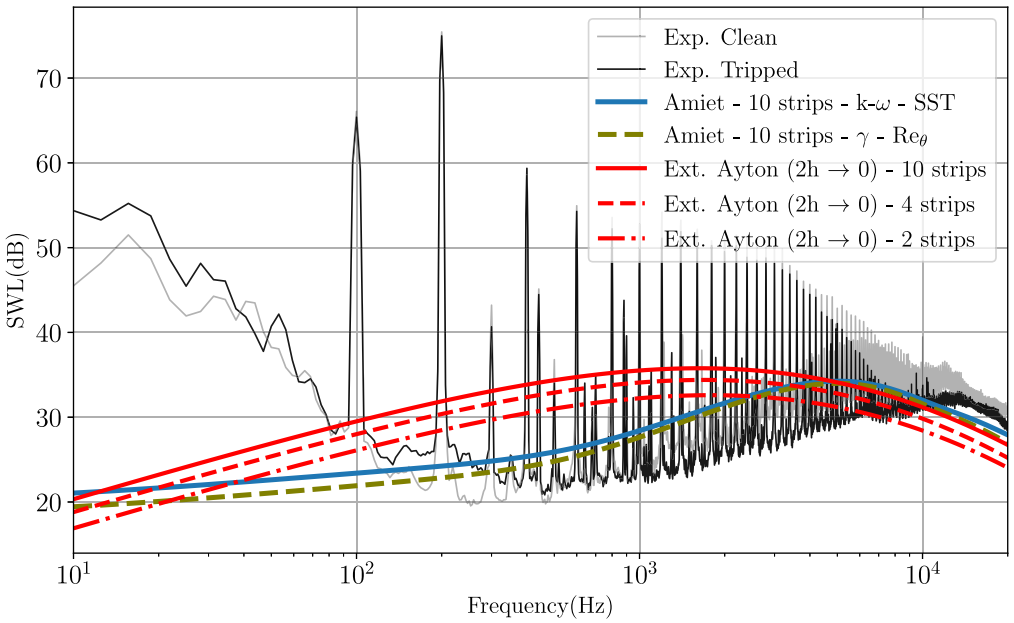

Fig. 13. Comparison of SWL from RANS-PyFanNoise using Amiet's and the extended Ayton's model with experimental data from clean and tripped propellers at 6000 RPM. (For interpretation of the references to color in this figure legend, the reader is referred to the web version of this article.)

noise was extracted as in Zawodny et al. [3]. Fig. 15 shows the overall sound pressure level (OASPL) directivity for the 4000, 6000, and 8000 RPM cases. The flow is from top to bottom with the rotational plane at 0°. On the one hand, Amiet's model captures the expected dipolar pattern due to trailing edge noise while the extended Ayton's model matches Amiet's model at high elevation angles from the rotor plane in agreement with the results of Section 2. On the other hand, the results from both models are in better agreement with the experimental data as the rotational speed increases; this follows the findings of the development of the boundary layer as shown in Fig. 11.

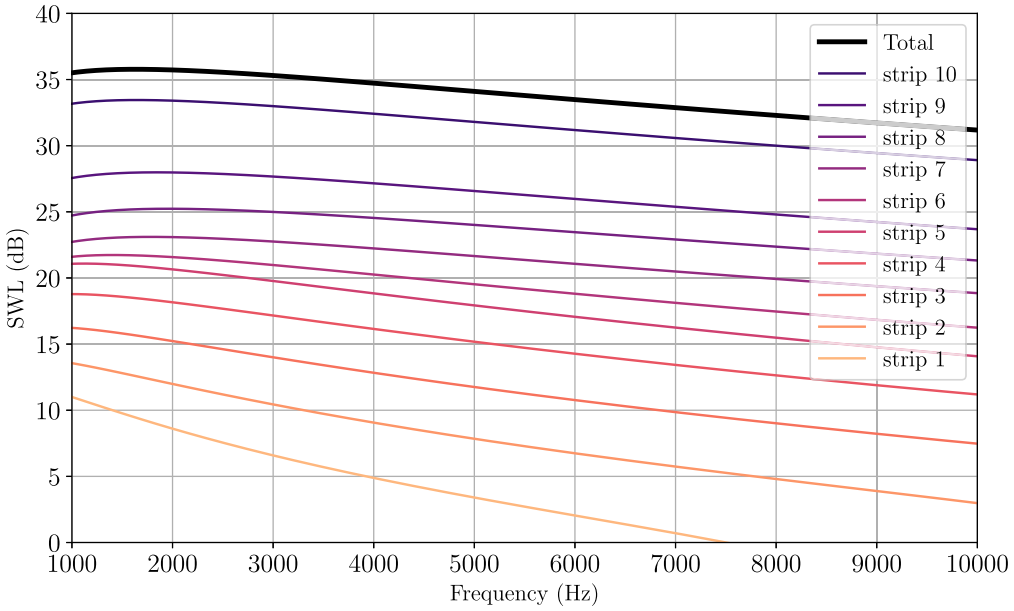

Fig. 14. Acoustic power radiated from each blade strip using Ayton's model.

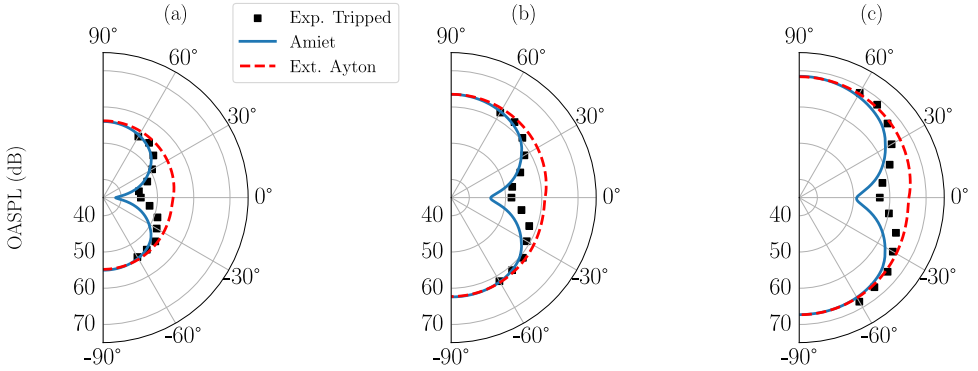

Fig. 15. OASPL directivity at 4000 (a), 6000 (b), and 8000 (c) RPM for a straight edge propeller using Amiet's and the extended Ayton's model. The flow is from top to bottom.

4.3. Acoustic results: serrated edge

In this section, the performance of different serration shapes on the NACA0012 drone propeller is investigated. According to [5,66], a serration becomes effective for amplitudes on the order of the boundary layer thickness ($2h \approx \delta$). Without loss of generality, the 6000 RPM case is chosen as the baseline. At this rotational speed, the boundary layer close to the tip is about 2.5 mm; thus, the serrations amplitude, unless otherwise noted, is 5 mm (20% of the chord). The serration amplitude-to-wavelength ratio $2h/\lambda$ is fixed to 2, in this case, following the optimal ratio found both experimentally and numerically [66,67].

Firstly, the noise levels of the propeller with sawtooth, sinusoidal, slitted-V, and square wave trailing edges are compared in Fig. 16 with the noise levels of the propeller with a straight edge. Note that the spectra are zoomed in the frequency range of 1 kHz to 10 kHz, where the attenuation occurs and where the models were in good agreement with the experimental data as shown. A linear scale is used for this decade. The slitted-V shape has the worst acoustic performance and the square wave the best with the sawtooth and sinusoidal shapes radiating almost equally across the spectrum. Given that all other inputs are identical, the difference in the spectrum for each shape is only caused by the modal expansion coefficients E_n.

The fact that the square wave performs better than the other shapes is surprising. The results from Section 3 showed that the square wave performs the worst in the cooling fan and wind turbine cases. To understand why the square wave outperforms all the other shapes for the NACA0012 propeller it is necessary to look in depth at the expansion coefficients, $E_n(\Lambda)$.

Fig. 17 shows the magnitude of the zeroth-mode expansion coefficient as a function of frequency for different shapes and an observer above the trailing edge. The Mach number and velocity values are taken from the propeller's outermost strip since it

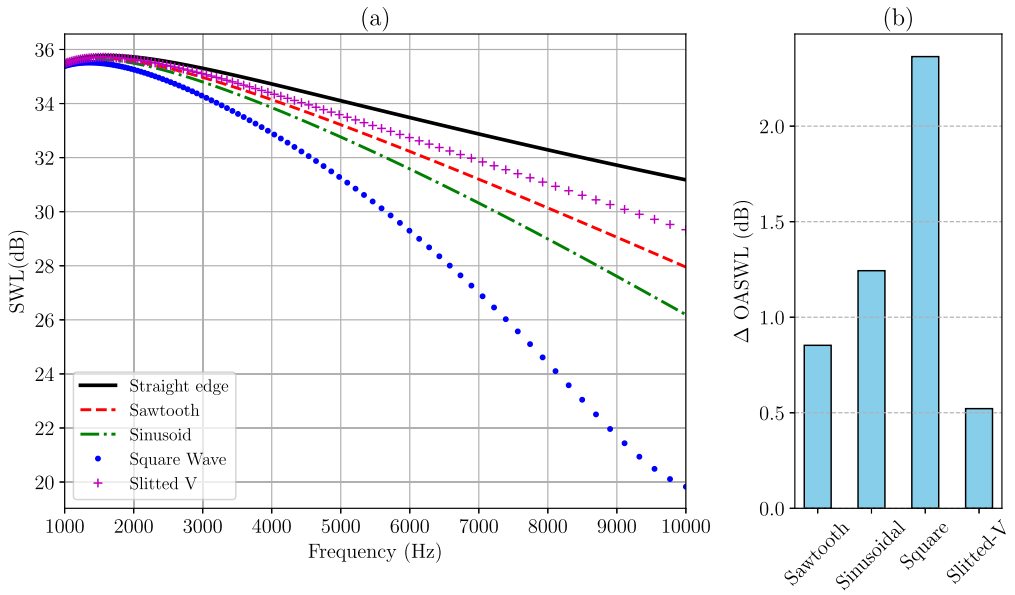

Fig. 16. (a) Acoustic power radiated from the drone propeller with different serration shapes and (b) OASWL reduction between straight edge and serrated edge configurations.

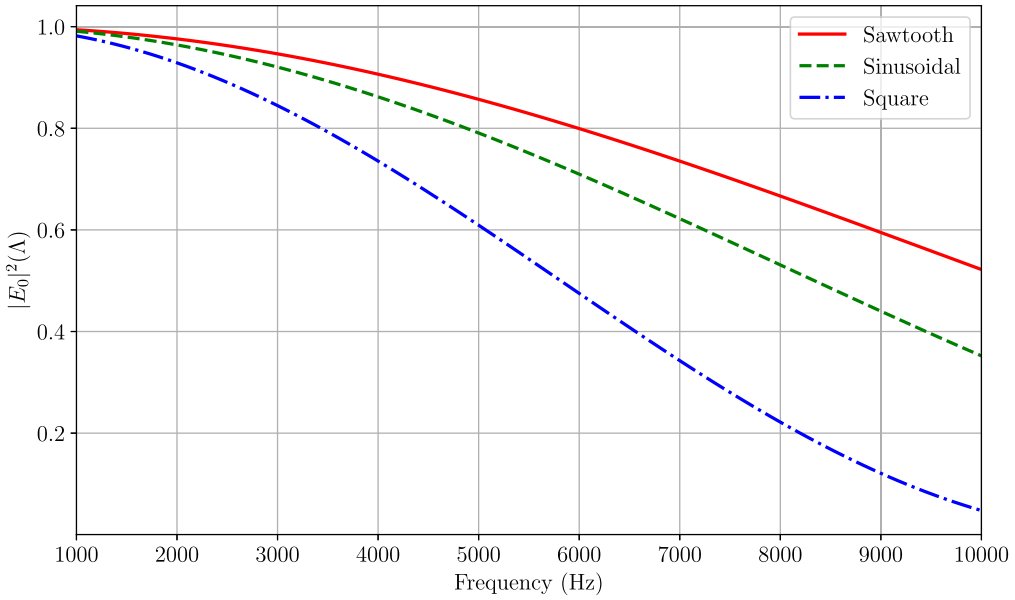

Fig. 17. Zeroth-mode expansion coefficient for different shapes for the NACA0012 propeller case.

contributes the most to the far-field. The curves follow the trend shown in the acoustic power spectrum (Fig. 16) and demonstrate that the square wave shape indeed outperforms the other ones. The zeroth-mode coefficient for the square wave is given by a cosine function (see Appendix B) and thus it can be shown that it will have maxima/minima for values of $\Lambda = 2n\pi$. For low Mach numbers and an observer above the trailing edge, this is in perfect agreement with the experimental results from Woodhead et al. [68] where the peaks/troughs were measured at frequencies $f = U_c/(2h)St$ for an airfoil with square-wave-type (slits) serrations and where St is the Strouhal number. Physically, this behavior comes from the constructive/destructive interference between the scattered waves from the root and the tip.

Contrary to the straight-edge case, the radiated acoustic power for serrated propellers might depend on more than the outermost strips. Fig. 18 shows the acoustic power radiated from each strip with square wave serrations. It can be seen that the local minimum at 10 kHz is due to the contribution from strips 4–8; thus how strips overlap is fundamental to understanding the shape of the total spectrum.

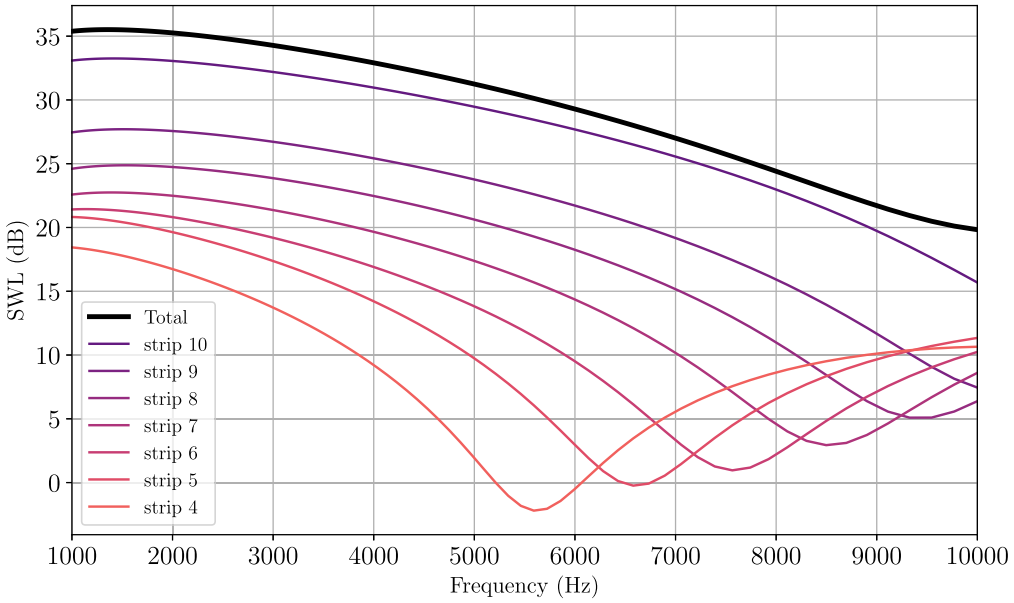

Fig. 18. Acoustic power radiated from each strip for a propeller with square wave serrations.

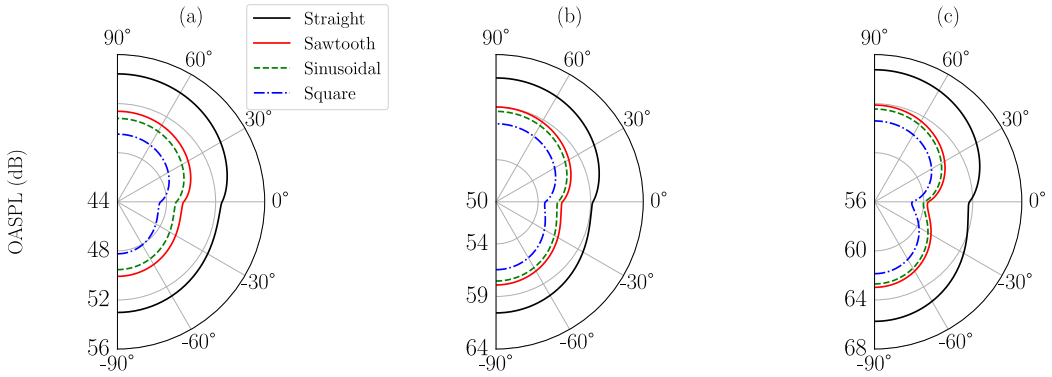

Fig. 19. OASPL directivity for different serration shapes at 4000 (a), 6000 (b), and 8000 RPM (c).

Since the serration height for a given propeller may be a fixed parameter once the blade is manufactured, it is important to calculate the noise reductions over the whole operational range of the propeller. This is even more important if square wave serrations are to be used since a change in RPM could trigger a phase shift close to or at the constructive interference region. Fig. 19 shows the directivity of the OASPL in the frequency range of 1–10 kHz for different serration shapes at different RPMs. It is clear that the serration height of 5 mm is effective over the whole operating points and for all observer angles. Additionally, it is noted that no lobes are present in any case, this is in good agreement with the original results in Ayton [32] where lobes appeared for values of $k(2h) > 4$ for the square wave and $k(2h) > 8$ for the sawtooth. In the present calculations, $k(2h)$ was always less than unity for the NACA0012 drone propeller.

The results for the NACA0012 drone propeller show that the square wave outperforms other serration shapes with the same amplitude and wavelength. Considering the typical tip Mach number range of drone propellers (0.15–0.3) and that a serration amplitude that would not impact the aerodynamics would be on the order of a few millimeters, the square wave has an interesting practical potential for small UAV propellers.

5. Applications to other UAVs

Given the limited range of applicability of the square wave type serration to small propellers, it is worth investigating alternatives for larger chord propellers, such as those found in ducted fans UAVs where diameter size constraints may play a key role and low-aspect ratio blades would be more appropriate [69,70]. For such designs, the chord length is necessarily larger than for the

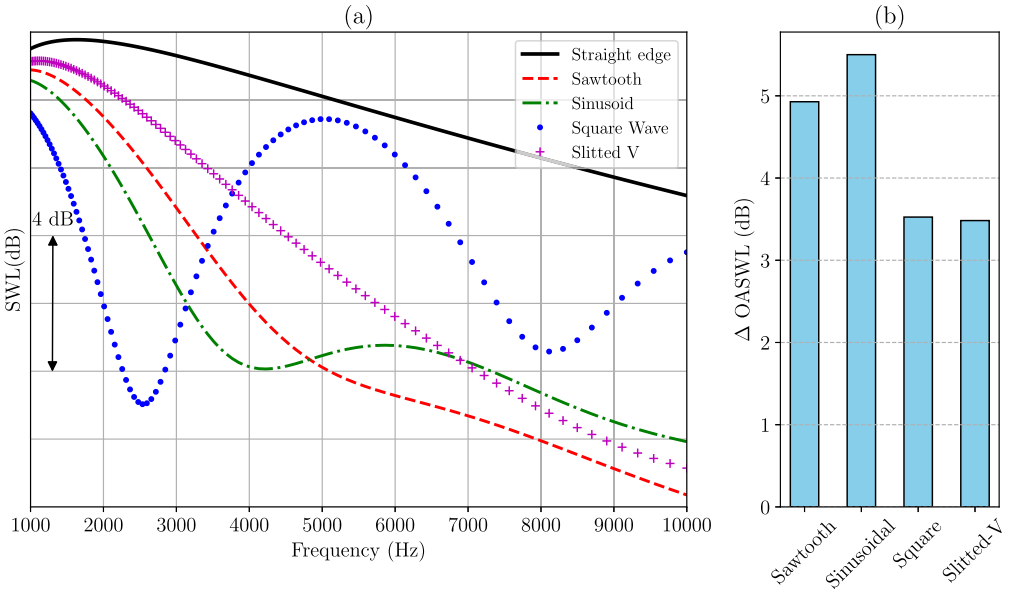

Fig. 20. (a) Acoustic power radiated from large-planform UAVs with different serration shapes and (b) OASWL reduction between straight edge and serrated edge configurations.

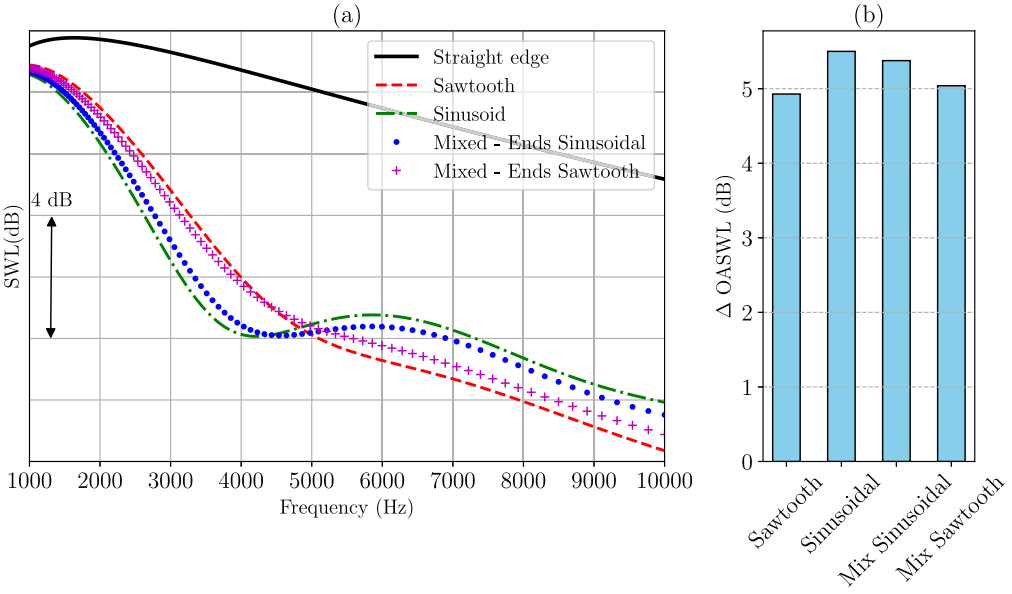

Fig. 21. (a) Acoustic power radiated from large-planform UAVs with mixed serration shapes and (b) OASWL reduction between straight edge and serrated edge configurations.

drone propellers discussed in the previous section, to achieve the required thrust. This allows longer serrations to be used without compromising aerodynamic performance.

First, a design where only the chord length is increased four-fold compared to the previous NACA0012 drone propeller is considered. Thus, a similar blade but with a larger chord such that the serration height-to-chord ratio remains the same is analyzed. The tip Mach number is also preserved, but the tip Reynolds number based on the chord length is now four times higher, which makes the previous fully turbulent RANS flow field simulation even more relevant. As for the drone propeller case, the noise levels for different serrated trailing edges are first compared in Fig. 20 with the noise levels of the same rotor with a straight edge (solid black line). Compared to Fig. 16 for the drone propeller, a very different picture emerges in the frequency range of interest and more significant noise reductions are observed. On the one hand, the square wave presents strong oscillations and no longer provides any benefit beyond 3 kHz. On the other hand, both the sawtooth and sinusoidal serrations effectively reduce noise levels on the whole

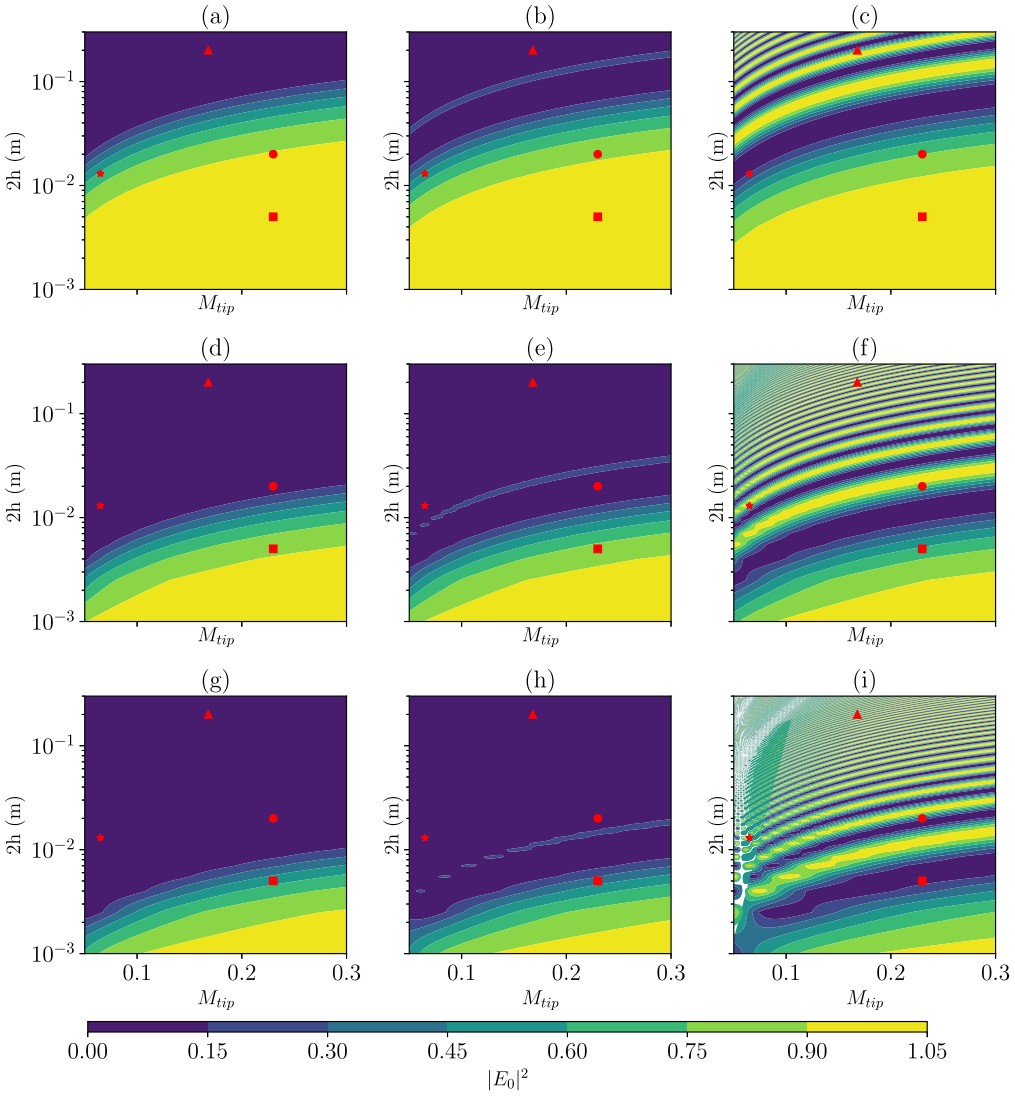

Fig. 22. Magnitude of the zeroth-mode expansion coefficient for the sawtooth [(a),(d) and (g)], sinusoidal [(b),(e) and (h)], and square wave [(c),(f) and (i)] serrations for 1000 Hz, [(a)–(c)], 5000 Hz, [(d)–(f)] and 10 000 Hz [(g)–(i)]. Wind turbine (△), cooling fan(*), drone propeller (□) and ducted fan(○). (For interpretation of the references to color in this figure legend, the reader is referred to the web version of this article.)

frequency range, by up to 8 dB at high frequencies. However, the frequencies at which they do so differ. The sawtooth outperforms the sinusoidal serration shape at frequencies greater than 5 kHz, whereas the opposite is true at lower frequencies. Given that all other inputs are identical, this effect is only caused by the modal expansion coefficients E_n. Moreover, an alternating pattern can be used along the span to obtain the best from both. Given that the last strip is expected to contribute the most to the far-field acoustics, as shown for the drone propeller case in Fig. 14, two configurations, one ending with sinusoidal serrations and the other with sawtooth serration for the outermost strip, are considered in Fig. 21. By blending the serrations, the noise reductions are seen to be slightly modified from the single-shape cases, and the shift to higher frequency can be subjectively beneficial and exploited to tailor the spectrum around the dominant trailing edge noise frequency.

If we now turn to more general design considerations where not only the chord length but also the diameter and the rotational speed can change, both the tip Mach number and Reynolds number based on the chord will vary. If we still consider that the design conditions will correspond to attached flow with flow features similar to Figs. 10 to 12, we can expect the noise reduction achieved by serrations to be driven again by their diffraction effect and therefore by the modal expansion coefficients E_n. Contours of the magnitude of the zeroth-mode expansion coefficients of the sawtooth, sinusoidal, and square-wave serrations are therefore presented in Fig. 22 as a function of the serration length $2h$ (in meter) and the tip Mach number M_{tip}, at selected frequencies of interest. In Fig. 22 the symbols represent the applications considered in this paper. For the wind turbine and cooling fan case, a serration height

of 10% of the chord is used. These contours for the square wave clearly show that it outperforms the other shapes at moderate tip Mach number and for serration heights less than 1 cm. As soon as the latter is beyond 1 cm, the sawtooth and sinusoidal serrations outperform the square wave (or slit), with either one providing the largest noise reduction depending on the frequency range. As shown above, this suggests a possible combination of these two serration types to achieve the broadest noise reduction over the whole frequency range of interest. Finally, an augmentation of the tip Mach number significantly reduces the effect of all serration designs for a given serration height. The latter needs to be doubled when the Mach number goes from 0.1 (small drones) to 0.4 (large UAM propellers).

6. Conclusions and perspectives

A low-order methodology has been presented showing potential noise reductions for a representative drone propeller. Li and Lee's extension of Ayton's model, coupled with Schlinker and Amiet's method for propellers, was validated for an industrial CD airfoil and wind turbine and cooling fan blade elements. The extended Ayton's model matches Amiet's model at high frequencies and for high elevation angles from the rotor plane. The directivity is typical of the half-plane solution.

Following single-blade passage RANS simulations of a small propeller with constant chord and pitch based on the NACA0012 airfoil, the wall-pressure fluctuations spectrum is modeled and the propeller far-field acoustics are calculated with the in-house code PyFanNoise. The acoustic results agree fairly with experimental measurements, especially at high rotational speeds, where secondary flows are weaker and the onset of turbulence matches more favorably with the fully turbulent k-ω SST model used in the RANS.

The extended Ayton's model was used to assess potential trailing edge noise reductions. It was shown that different serration shapes perform better at different non-dimensional frequencies. The often-overlooked square wave was shown to outperform the more traditional sawtooth and sinusoidal serrations when used in the NACA0012 drone propeller, over the whole operational range. The OASPL directivity plots showed no lobes for any of the shapes considered and reductions of up to 10 dB are possible with the square wave at high frequencies. Larger noise reductions and a larger design space for the serrations can be obtained by increasing the blade planforms allowing longer more efficient serrations. Indeed, a mixed of sinusoidal and sawtooth serrations can then be tuned to achieve significant noise reduction over the entire audible frequency range of interest between 100 Hz and 10 kHz. This could also change the classical propeller design paradigm where the blade chord distribution and planform should be no longer driven by aerodynamic considerations first but by passive noise reduction constraints.

Future improvements to the present methodology might come from two fronts. Firstly, the inclusion of low-order transitional models has already been shown to provide a better agreement on aerodynamic quantities and give a more accurate description of the state of the boundary layer over the rotor blade and consequently close to the trailing edge. However, extensions of the models for wall-pressure statistics are still needed. Secondly, while the extended Ayton's model gives good insights, more precise calculations require the development of more accurate transfer functions for different shapes as shown by Lyu [71]. Lastly, it is worth mentioning that accounting for the relationship between serration shape and spanwise wall-pressure correlation length could lead to further noise reductions as shown by Kholodov and Moreau [67].

CRediT authorship contribution statement

Jorge Santamaria: Writing – review & editing, Writing – original draft, Visualization, Validation, Software, Investigation, Formal analysis, Data curation, Conceptualization. **André Bierrenbach-Lima:** Visualization, Formal analysis, Data curation. **Marlène Sanjosé:** Writing – review & editing, Writing – original draft, Supervision, Software, Resources, Project administration, Methodology, Funding acquisition, Formal analysis, Data curation, Conceptualization. **Stéphane Moreau:** Writing – review & editing, Writing – original draft, Validation, Supervision, Project administration, Methodology, Formal analysis, Data curation, Conceptualization.

Declaration of competing interest

The authors declare that they have no known competing financial interests or personal relationships that could have appeared to influence the work reported in this paper.

Acknowledgments

The authors acknowledge the Digital Research Alliance of Canada for providing the necessary computational resources for this research. J. Santamaria is thankful for the support from the FRQNT - PR 300387. The authors acknowledge the partners of the UHEQ Consortium II and III at Université de Sherbrooke, which develops and provides the acoustic software PyFanNoise for this research. Additionally, the authors acknowledge Dr. Romain Gojon and Dr. Gyuzel Yakhina for experimental data on the NACA0012 propeller and the CD airfoil respectively.

Appendix A. Aeroacoustic transfer functions

The aeroacoustic transfer function, sometimes referred to as acoustic lift, in Amiet's model, Eq. (1) is given by:

$$I = \frac{\mathrm{i}}{C}\left\{\sqrt{\frac{B}{B-C}}\,\mathrm{erf}\left(\sqrt{2\mathrm{i}(B-C)}\right) + e^{\mathrm{i}2C}\left[1-\mathrm{erf}\left(\sqrt{2\mathrm{i}B}\right)\right]\right\} \tag{A.1}$$

where $B = (k_x + M\mu + \kappa)c/2$ and $C = k_x c/2 - \mu(x/S_0 - M)$ with $\mu = k/\beta^2(c/2)$ and $\kappa^2 = \mu^2 - (k_y/\beta)^2$

For serrated edges, the modal expansion coefficients in Ayton's model, Eq. (6), serve the role of the aeroacoustic transfer function and depend on the shape. For sawtooth edges are given by:

$$E_n^{\mathrm{saw}}(\Lambda) = \frac{-4\Lambda e^{-\mathrm{i}n\pi}}{4n^2\pi^2 - \Lambda^2}\sin\left(\frac{1}{4}(\Lambda + 2n\pi)\right) \tag{A.2}$$

for square wave:

$$E_n^{\mathrm{sq}}(s) = \begin{cases} \frac{\mathrm{i}e^{\mathrm{i}(n-1)\pi/2}}{n\pi}\sin(\frac{\Lambda}{4}) & n \quad \text{odd} \\ 0 & n \quad \text{even} \\ \cos(\frac{\Lambda}{4}) & n \quad 0 \end{cases} \tag{A.3}$$

for sinusoidal shapes:

$$E_n^{\mathrm{sin}}(\Lambda) = J_{-n}(-\Lambda/4) \tag{A.4}$$

where $\Lambda = (k_x + kM/\beta^2 - k_n\cos\Theta)2h/\beta$ and J_n is the Bessel's function of nth order of the first kind.

Appendix B. Wall-pressure models parameters

For the Chou and George [43] model, the boundary layer displacement thickness is given by:

$$\delta^*/c = \begin{cases} (24.3 + 0.6625x_a)10^{-4} & x_a \le 4° \\ (26.95 + 0.6625(x_a - 4) + 0.3044(x_a - 4)^2 & \\ \quad + 0.0104(x_a - 4)^3)10^{-4} & x_a > 4° \end{cases} \tag{B.1}$$

where x_a is the angle of attack and the spectrum function $F(\bar{\omega})$ is given by

$$F(\bar{\omega}) = \begin{cases} \dfrac{1.732\times10^{-3}\bar{\omega}}{1 - 5.489\bar{\omega} + 36.74\bar{\omega}^2 + 0.1505\bar{\omega}^5} & \bar{\omega} < 0.06 \\ \dfrac{1.4216\times10^{-3}\bar{\omega}}{0.3261 + 4.1837\bar{\omega} + 22.818\bar{\omega}^2 + 0.0013\bar{\omega}^3 + 0.0028\bar{\omega}^5} & \bar{\omega} \ge 0.06 \end{cases} \tag{B.2}$$

The parameters to model the wall-pressure spectrum in Eq. (5) using Rozenberg's and Lee's model are given in Tables B.1 to B.3: where $\Delta = \delta/\delta^*$ and $\Pi = 0.8(\beta_c + 0.5)^{3/4}$ is Cole's wake parameter computed by an explicit formulation [60]

Table B.1
Parameters a-c for empirical wall-pressure spectrum models.

	a	b	c
Rozenberg	$[2.82\Delta^2(6.13\Delta^{-0.75} + d)^e][4.2(\Pi/\Delta)+1]$	2	0.75
Lee	$\max(a_{Roz}, (0.25\beta_c - 0.52)a_{Roz})$	2	0.75

Table B.2
Parameters d-g for empirical wall-pressure spectrum models.

	d	e	f	g
Rozenberg	$4.76(1.4/\Delta)^{0.75}[0.375e - 1]$	$3.7+1.5\beta_c$	8.8	−0.57
Lee	$\max(1, 1.25d_{Roz})(\beta_c < 0.5)$ or $d_{Roz}(\beta_c \ge 0.5)$	$3.7+1.5\beta_c$	8.8	−0.57

Table B.3
Parameters h-i, spectrum, and frequency scaling for empirical wall-pressure spectrum models.

	h	i	SS	FS
Rozenberg	$\min(3, 19/\sqrt{R_T})+4$	4.76	$U_e/\tau_{max}^2\delta^*$	δ^*/U_e
Lee	$\min(3, (0.139+3.1043\beta_c))+7$	4.76	$U_e/\tau_w^2\delta^*$	δ^*/U_e

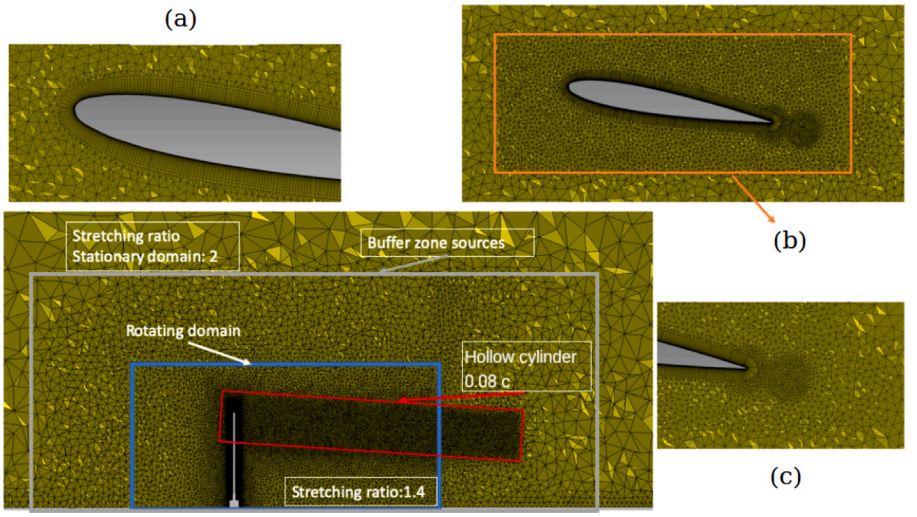

Fig. C.1. Mesh strategy showing zones of refinement for the leading edge (a), the blade near-field (b) and the trailing edge (c).

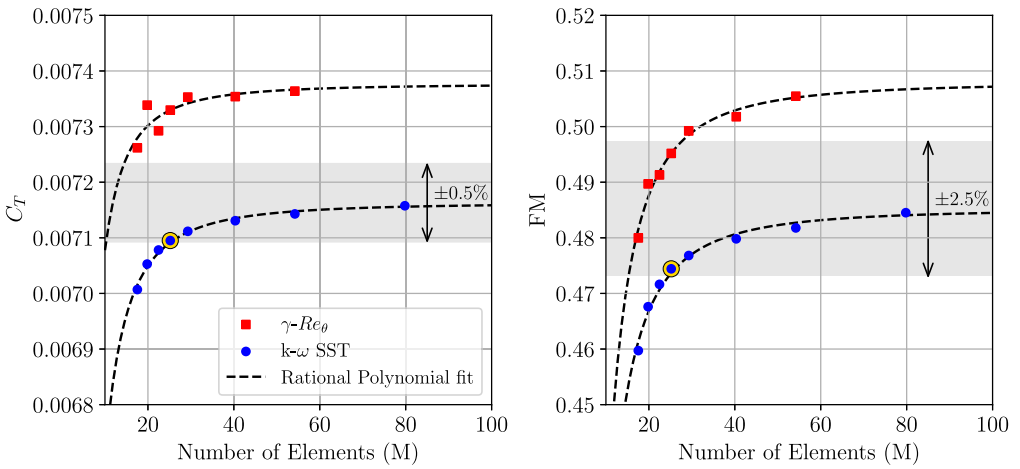

Fig. C.2. Mesh convergence for (a) thrust coefficient and for (b) Figure of Merit as a function of cell number given in million (M). (For interpretation of the references to color in this figure legend, the reader is referred to the web version of this article.)

Appendix C. Mesh convergence study

Since the boundary layer parameters are essential for predicting trailing-edge noise, the meshing strategy was initially directed to the blade with sufficient refinement to capture the boundary layer within the prismatic layer. This strategy resulted in an underprediction of the thrust by almost 15%. A more global strategy is required to improve performance predictions. Based on the results of Ruiz et al. [61], the following approach was taken. First, a smaller stretching ratio in the rotational domain was adopted resulting in less dissipation of the propeller wake. Secondly, a local refinement was used to capture the tip vortex system with an average tetrahedral element size of 2 mm (10% of the chord). Finally, the maximum tetrahedral size of in the entire domain was limited to 50 mm (40% of the propeller diameter). Fig. C.1 shows a meridional view of the mesh with the refinements in the near-field of the blade and the propeller.

The effectiveness of this meshing strategy is assessed by computing the thrust and torque coefficients together with the Figure of Merit in several meshes obtained by scaling a baseline mesh of about 20 million elements. Fig. C.2 shows the convergence of the thrust coefficient and Figure of Merit with increasing number of elements provided in millions. A rational function of the form $f(x) = \frac{a}{x^2} + b$ with x being the number of cells in the mesh and b the asymptotic value has been added to highlight the converging trend. The shaded areas represent a margin of 1% and 5% centered on the asymptotic values obtained with the polynomial fits for C_T and FM respectively. This highlights the importance of resolving not only the boundary layers on the blade but also the correct trajectory and dissipation of the tip vortices in hovering. The selected mesh is highlighted in yellow as a compromise between

simulation accuracy and simulation cost. The obtained performances for the selected mesh are within 0.5% an 2.5% of the asymptotic values of C_T and FM respectively. The convergence of the transitional simulations is not as regular as with the fully turbulent simulations. This can be associated to more sensitivity of the transitional model to grid resolution.

Data availability

Data will be made available on request.

References

[1] C.S. Thurman, N.S. Zawodny, J.D. Baeder, Computational prediction of broadband noise from a representative small unmanned aerial system rotor, in: VFS Int 76th Ann Forum, 2020.
[2] N.A. Pettingill, N.S. Zawodny, C. Thurman, L.V. Lopes, Acoustic and performance characteristics of an ideally twisted rotor in hover, in: AIAA SCITECH 2021 Forum, 2021, p. 1928.
[3] N.S. Zawodny, D.D. Boyd Jr., C.L. Burley, Acoustic characterization and prediction of representative, small-scale rotary-wing unmanned aircraft system components, in: AHS Annual Forum, NF1676L-22587, 2016.
[4] G. Romani, E. Grande, F. Avallone, D. Ragni, D. Casalino, Performance and noise prediction of low-reynolds number propellers using the lattice-Boltzmann method, Aerosp. Sci. Technol. 125 (2022) 107086.
[5] S. Lee, L. Ayton, F. Bertagnolio, S. Moreau, T.P. Chong, P. Joseph, Turbulent boundary layer trailing-edge noise: Theory, computation, experiment, and application, Prog. Aerosp. Sci. 126 (2021) 100737.
[6] S. Oerlemans, M. Fisher, T. Maeder, K. Kögler, Reduction of wind turbine noise using optimized airfoils and trailing-edge serrations, AIAA J. 47 (2009) 1470–1481.
[7] Z. Ning, R.W. Wlezien, H. Hu, An experimental study on small uav propellers with serrated trailing edges, in: 47th AIAA Fluid Dyn Conf, 2017, p. 3813.
[8] E. Pang, A. Cambray, D. Rezgui, M. Azarpeyvand, S.A. Showkat Ali, Investigation towards a better understanding of noise generation from uav propellers, in: 24th AIAA/CEAS Aeroacoust Conf, 2018, p. 3450.
[9] Y. Yang, Y. Wang, Y. Liu, H. Hu, Z. Li, Noise reduction and aerodynamics of isolated multi-copter rotors with serrated trailing edges during forward flight, J. Sound Vib. 489 (2020) 115688.
[10] H. Tian, B. Lyu, Prediction of broadband noise from rotating blade elements with serrated trailing edges, Phys. Fluids 34 (2022) 085109.
[11] M.J. Lighthill, On sound generated aerodynamically i. general theory, Proc. R. Soc. Lond. Ser. A Math. Phys. Eng. Sci. 211 (1952) 564–587.
[12] A. Powell, On the aerodynamic noise of a rigid flat plate moving at zero incidence, J. Acoust. Soc. Am. 31 (1959) 1649–1653.
[13] J.E. Ffowcs Williams, L.H. Hall, Aerodynamic sound generation by turbulent flow in the vicinity of a scattering half plane, J. Fluid Mech. 40 (1970) 657–670.
[14] M.S. Howe, A review of the theory of trailing edge noise, J. Sound Vib. 61 (1978) 437–465.
[15] R.K. Amiet, Noise due to turbulent flow past a trailing edge, J. Sound Vib. 47 (1976) 387–393.
[16] T.F. Brooks, D.S. Pope, M.A. Marcolini, Airfoil Self-Noise and Prediction, Technical Report, National Aeronautics and Space Administration, 1989.
[17] F. Bertagnolio, A. Fischer, C. Appel, M. Herr, F. Seel, T. Lutz, K. Boorsma, G. Schepers, M. Botero, D. Casalino, W. van der Velden, C. Sucameli, P. Bortolotti, Wind turbine noise code benchmark: A comparison and verification exercise, in: 10th Int Conf Wind Turb Noise, Dublin, Ireland, 2023.
[18] M. Roger, S. Moreau, Back-scattering correction and further extensions of amiet's trailing-edge noise model. Part 1: theory, J. Sound Vib. 286 (2005) 477–506.
[19] D.R. Neal, The Effects of Rotation on the Flow Field over a Controlled-Diffusion Airfoil, Michigan State University, 2010.
[20] M.K. Bull, Wall-pressure fluctuations beneath turbulent boundary layers: some reflections on forty years of research, J. Sound Vib. 190 (1996) 299–315.
[21] M. Goody, Empirical spectral model of surface pressure fluctuations, AIAA J. 42 (2004) 1788–1794.
[22] Y. Rozenberg, G. Robert, S. Moreau, Wall-pressure spectral model including the adverse pressure gradient effects, AIAA J. 50 (2012) 2168–2179.
[23] S. Lee, Empirical wall-pressure spectral modeling for zero and adverse pressure gradient flows, AIAA J. 56 (2018) 1818–1829, http://dx.doi.org/10.2514/1.J056528.
[24] M. Sanjosé, C. Méon, S. Moreau, A. Idier, P. Laffay, Direct numerical simulation of acoustic reduction using serrated trailing-edge on an isolated airfoil, in: 20th AIAA/CEAS Aeroacoust Conf, 2014, p. 2324.
[25] L. Jones, R. Sandberg, Acoustic and hydrodynamic analysis of the flow around an aerofoil with trailing-edge serrations, J. Fluid Mech. 706 (2012) 295–322.
[26] S. Moreau, M. Sanjosé, B. Lyu, L.J. Ayton, Analytical, numerical and experimental investigation of trailing-edge noise reduction on a controlled diffusion airfoil with serrations, in: 25th AIAA/CEAS Aeroacoust Conf, 2019, p. 2450.
[27] M. Sanjosé, S. Moreau, Fast and accurate analytical modeling of broadband noise for a low-speed fan, J. Acoust. Soc. Am. 143 (2018) 3103–3113, http://dx.doi.org/10.1121/1.5038265.
[28] D. Lallier-Daniels, F. Bolduc-Teasdale, D. Rancourt, S. Moreau, Fast multi-objective aeroacoustic optimization of propeller blades, in: VFS Int 77th Ann Forum, Vertical Flight Society, Virtual, 2021, p. 13.
[29] M.S. Howe, Aerodynamic noise of a serrated trailing edge, J. Fluid Struct. 5 (1991) 33–45.
[30] M. Gruber, P. Joseph, T.P. Chong, Experimental investigation of airfoil self noise and turbulent wake reduction by the use of trailing edge serrations, in: 16th AIAA/CEAS Aeroacoust Conf, 2010, p. 3803.
[31] B. Lyu, M. Azarpeyvand, S. Sinayoko, Prediction of noise from serrated trailing edges, J. Fluid Mech. 793 (2016) 556–588.
[32] L.J. Ayton, Analytic solution for aerodynamic noise generated by plates with spanwise-varying trailing edges, J. Fluid Mech. 849 (2018) 448–466.
[33] B. Lyu, L.J. Ayton, Rapid noise prediction models for serrated leading and trailing edges, J. Sound Vib. 469 (2020) 115136.
[34] R. Schlinker, R. Amiet, Helicopter rotor trailing edge noise, in: 7th AIAA/CEAS Aeroacoust Conf, 1981, p. 2001.
[35] S. Sinayoko, M. Kingan, A. Agarwal, Trailing edge noise theory for rotating blades in uniform flow, Proc. R. Soc. Lond. Ser. A Math. Phys. Eng. Sci. 469 (2013) 20130065, http://dx.doi.org/10.1098/rspa.2013.0065.
[36] Y. Rozenberg, M. Roger, S. Moreau, Rotating blade trailing-edge noise: Experimental validation of analytical model, AIAA J. 48 (2010) 951–962.
[37] A. Halimi, B.G. Marinus, S. Larbi, Analytical prediction of broadband noise from mini-rpa propellers with serrated edges, Int. J. Aeroacoust. 18 (2019) 517–535.
[38] S. Li, S. Lee, Extensions and applications of lyu and ayton's serrated trailing-edge noise model to rotorcraft, in: 28th AIAA/CEAS Aeroacoust Conf, 2022, p. 2916.
[39] R.K. Amiet, Acoustic radiation from an airfoil in a turbulent stream, J. Sound Vib. 41 (1975) 407–420.
[40] L.J. Ayton, J.R. Gill, N. Peake, The importance of the unsteady kutta condition when modelling gust–aerofoil interaction, J. Sound Vib. 378 (2016) 28–37.
[41] N. Curle, The influence of solid boundaries upon aerodynamic sound, Proc. R. Soc. Lond. Ser. A Math. Phys. Eng. Sci. 231 (1955) 505–514.

[42] G. Corcos, The structure of the turbulent pressure field in boundary-layer flows, J. Fluid Mech. 18 (1964) 353–378.
[43] S.-T. Chou, A. George, Effect of angle of attack on rotor trailing-edge noise, AIAA J. 22 (1984) 1821–1823.
[44] L.J. Ayton, P. Chaitanya, An analytical and experimental investigation of aerofoil–turbulence interaction noise for plates with spanwise-varying leading edges, J. Fluid Mech. 865 (2019) 137–168.
[45] J. Santamaria, M. Sanjose, S. Moreau, Fast broadband noise prediction of serrated uav rotors in hover, in: AIAA SCITECH 2023 Forum, 2023, p. 0618.
[46] M. Roger, S. Moreau, A. Guedel, Broadband fan noise prediction using single-airfoil theory, Noise Control Eng. J. 54 (2006).
[47] Y. Tian, B. Cotté, Wind turbine noise modeling based on amiet's theory: Effects of wind shear and atmospheric turbulence, Acta Acust. United Acust. 102 (2016) 626–639.
[48] L. Bouma, M. Malbois, A.C. Bresciani, J. Maillard, S. Moreau, L.D. de Santana, Far-field propagation of wind turbine noise using the harmonoise model, in: AIAA AVIATION 2023 Forum, 2023, p. 3645.
[49] S. Moreau, M. Henner, G. Iaccarino, M. Wang, M. Roger, Analysis of flow conditions in freejet experiments for studying airfoil self-noise, AIAA J. 41 (2003) 1895–1905.
[50] M. Wang, S. Moreau, G. Iaccarino, M. Roger, Les prediction of wall-pressure fluctuations and noise of a low-speed airfoil, Int. J. Aeroacoust. 8 (2009) 177–197.
[51] S. Moreau, M. Roger, Effect of airfoil aerodynamic loading on trailing edge noise sources, AIAA J. 43 (2005) 41–52, http://dx.doi.org/10.2514/1.5578.
[52] T. Padois, P. Laffay, A. Idier, S. Moreau, Detailed experimental investigation of the aeroacoustic field around a controlled-diffusion airfoil, in: 21st AIAA/CEAS Aeroacoust Conf, American Institute of Aeronautics and Astronautics, 2019/03/04, 2015, http://dx.doi.org/10.2514/6.2015-2205.
[53] S. Moreau, P. Laffay, A. Idier, N. Atalla, Several noise control of the trailing-edge noise of a controlled-diffusion airfoil, in: 22nd AIAA/CEAS Aeroacoust Conf, Aeroacoustics Conferences, American Institute of Aeronautics and Astronautics, 2016, http://dx.doi.org/10.2514/6.2016-2816.
[54] H. Wu, S. Moreau, R.D. Sandberg, On the noise generated by a controlled-diffusion aerofoil at rec=1.5 ×105, J. Sound Vib. 487 (2020) 115620.
[55] A. Arroyo Ramo, S. Moreau, R.D. Sandberg, M. Bauerheim, M.C. Jacob, Controlled diffusion airfoil self-noise, an acoustic far-field prediction, in: AIAA AVIATION 2023 Forum, 2023, p. 3505.
[56] M.S. Howe, Edge-source acoustic green's function for an airfoil of arbitrary chord, with application to trailing-edge noise, Q. J. Mech. Appl. Math. 54 (2001) 139–155.
[57] V.P. Blandeau, P.F. Joseph, Validity of amiet's model for propeller trailing-edge noise, AIAA J. 49 (2011) 1057–1066.
[58] R. Gojon, T. Jardin, H. Parisot-Dupuis, Experimental investigation of low reynolds number rotor noise, J. Acoust. Soc. Am. 149 (2021) 3813–3829.
[59] J. Santamaria, M. Sanjose, R. Gojon, S. Belliot, S. Moreau, Installation and manufacturing effects of propeller trailing edge serrations, in: 30th AIAA/CEAS Aeroacoustics Conference (2024), Aeroacoustics Conferences, American Institute of Aeronautics and Astronautics, 2024, http://dx.doi.org/10.2514/6.2024-3322, URL: https://arc.aiaa.org/doi/10.2514/6.2024-3322.
[60] M. Sanjosé, S. Moreau, Fast and accurate analytical modeling of broadband noise for a low-speed fan, J. Acoust. Soc. Am. 143 (2018) 3103–3113.
[61] M.C. Ruiz, M. Scanavino, D. D'Ambrosio, G. Guglieri, A. Vilardi, Experimental and numerical analysis of hovering multicopter performance in low-reynolds number conditions, Aerosp. Sci. Technol. 128 (2022) 107777.
[62] C. Thurman, D.D. Boyd Jr., P. Buning, G. Reboul, C. Benoit, NASA/ONERA collaboration on small hovering rotor broadband noise prediction using lattice-Boltzmann method and structured Navier-Stokes solvers, in: 30th AIAA/CEAS Aeroacoustics Conference (2024), American Institute of Aeronautics and Astronautics, 2024, http://dx.doi.org/10.2514/6.2024-3106, URL: https://arc.aiaa.org/doi/abs/10.2514/6.2024-3106. _eprint: https://arc.aiaa.org/doi/pdf/10.2514/6.2024-3106.
[63] D. Casalino, G. Romani, L.M. Pii, R. Colombo, Flow confinement effects on sUAS rotor noise, Aerosp. Sci. Technol. 143 (2023) 108756, http://dx.doi.org/10.1016/j.ast.2023.108756.
[64] D. Shenoy, R. Gojon, T. Jardin, M. Jacob, Aerodynamic and acoustic study of a small scale lightly loaded hovering rotor using large eddy simulation, Aerosp. Sci. Technol. 150 (2024) 109219.
[65] S. Montoya-Ospina, F. Simon, R. Gojon, H. Parisot-Dupuis, Passive noise control for low reynolds number rotors, in: 30th AIAA/CEAS Aeroacoustics Conference (2024), 2024, p. 3112.
[66] M. Gruber, P. Joseph, T. Chong, On the mechanisms of serrated airfoil trailing edge noise reduction, in: 17th AIAA/CEAS Aeroacoust Conf, Aeroacoustics Conferences, American Institute of Aeronautics and Astronautics, 2011, http://dx.doi.org/10.2514/6.2011-2781.
[67] P. Kholodov, S. Moreau, Optimization of trailing-edge serrations with and without slits for broadband noise reduction, J. Sound Vib. 490 (2021) 115736, http://dx.doi.org/10.1016/j.jsv.2020.115736.
[68] P.C. Woodhead, T.P. Chong, P. Joseph, J. Wissink, On the double-rooted trailing edge serration, in: 25th AIAA/CEAS Aeroacoust Conf, 2019, p. 2436.
[69] S. Deng, S. Wang, Z. Zhang, Aerodynamic performance assessment of a ducted fan uav for vtol applications, Aerosp. Sci. Technol. 103 (2020) 105895.
[70] W. Graf, J. Fleming, W. Ng, Improving ducted fan uav aerodynamics in forward flight, in: 46th AIAA Aerosp Sci Meet, 2008, p. 430.
[71] B. Lyu, Analytical green's function for the acoustic scattering by a flat plate with a serrated edge, J. Fluid Mech. 961 (2023) A33.